

# High-resolution analyses of concentrations and sizes of refractory black carbon particles deposited on northwest Greenland over the past 350 years - Part 2: Seasonal and temporal trends in refractory black carbon originated from fossil fuel combustion and biomass burning

Kumiko Goto-Azuma<sup>1,2</sup>, Yoshimi Ogawa-Tsukagawa<sup>1</sup>, Kaori Fukuda<sup>1</sup>, Koji Fujita<sup>3</sup>, Motohiro Hirabayashi<sup>1</sup>, Remi Dallmayr<sup>1,a</sup>, Jun Ogata<sup>1</sup>, Nobuhiro Moteki<sup>4</sup>, Tatsuhiro Mori<sup>5</sup>, Sho Ohata<sup>3</sup>, Yutaka Kondo<sup>1</sup>, Makoto Koike<sup>6</sup>, Sumito Matoba<sup>7</sup>, Moe Kadota<sup>7</sup>, Akane Tsushima<sup>1,b</sup>, Naoko Nagatsuka<sup>1,c</sup>, and Teruo Aoki<sup>1</sup>

<sup>1</sup>National Institute of Polar Research, Tachikawa, Tokyo, 190-8518, Japan

<sup>2</sup>SOKENDAI, Shonan Village, Hayama, Kanagawa, 240-0193, Japan

<sup>3</sup>Nagoya University, Nagoya, 464-8601, Japan

<sup>4</sup>Tokyo Metropolitan University, Hachioji, Tokyo, 192-0397, Japan

<sup>5</sup>Keio University, Yokohama, Kanagawa, 223-8521, Japan

<sup>6</sup>University of Tokyo, Bunkyo-ku, Tokyo, 113-0033, Japan

<sup>7</sup>Hokkaido University, Sapporo, 060-0819, Japan

<sup>a</sup>Now at Alfred Wegener Institute for Polar and Marine Research, Bremerhaven, Germany

<sup>b</sup>Now at Nagasaki University, Nagasaki, 852-8521, Japan

<sup>c</sup>Now at Japan Agency for Marine-Earth Science and Technology, Yokosuka, Kanagawa, 237-061, Japan

Correspondence to: Kumiko Goto-Azuma (kumiko@nipr.ac.jp)

**Abstract.** The roles and impacts of refractory black carbon (rBC), an important aerosol species affecting Earth's radiation budget, are not well understood owing to lack of accurate long-term observations. To study the temporal changes in rBC since the pre-industrial period, we analysed rBC in an ice core drilled in northwest Greenland. Using an improved technique for rBC measurement and a continuous flow analysis system, we obtained accurate and high temporal resolution records of rBC particle size and mass/number concentrations for the past 350 years. Number and mass concentrations, which both started to increase in the 1870s associated with inflow of anthropogenically derived rBC, reached their maxima in the 1910s–1920s and then subsequently decreased. ~~On the basis of backward trajectory analyses, suggest we found~~ that North America was likely the dominant source region of the anthropogenic rBC in the ice core. The increase in anthropogenic rBC shifted the annual concentration peaks of rBC from summer to winter–early spring. After rBC concentrations diminished to pre-industrial levels, the annual peak concentration of rBC returned to the summer. We found that anthropogenic rBC particles were larger than

32 biomass burning rBC particles. By separating the rBC in winter and summer, we reconstructed the temporal variations in rBC  
33 that originated from biomass burning, including the period with large anthropogenic input. The rBC that originated from  
34 biomass burning showed no trend of increase until the early 2000s. Finally, possible albedo reductions due to rBC are discussed.  
35 Our new data provide key information for validating aerosol and climate models, thereby supporting improved projections of  
36 future climate and environment.

## 37 **1 Introduction**

38 Black carbon (BC) particles, which are emitted by incomplete combustion of biomass and fossil fuels, ~~play important roles~~  
39 ~~in~~ affect Earth's radiation budget and thus ~~in~~ climate change (Bond et al., 2013; Moteki, 2023; Matsui et al., 2022; Legrand et  
40 al., 2016). In turn, changes in climate can affect emissions of BC from biomass burning through natural processes such as  
41 wildfires. Global warming is considered a major cause of the recent increase in large wildfires globally that can cause serious  
42 damage to ecosystems and human society (Calkin et al., 2023; Keeley and Syphard, 2021; Wang et al., 2021; Keane et al.,  
43 2008). Increased occurrence of large wildfires in the future could affect Earth's radiation budget, and change the frequency at  
44 which certain regions are exposed to serious hazard. ~~Changes in~~ Increases of fossil fuel combustion since the Industrial  
45 Revolution have changed Earth's radiation budget and contributed to the warming or cooling over the past century (Shindell  
46 and Faluvegi, 2009; McConnell et al., 2007; Breider et al., 2017). To understand the effects of BC on the radiation budget and  
47 ~~of~~ the impact of climate change on BC emissions, the long-term changes in the concentrations and size distributions of BC  
48 particles should be known. Data obtained since the pre-industrial period are particularly valuable because we cannot fully  
49 understand the anthropogenic effects without characterizing BC in a pristine environment. The Arctic is the key region for  
50 clearer elucidation of the roles of BC because the Arctic has warmed at a rate four times faster than that of the global average  
51 over the past half century, leading to drastic changes such as sea ice retreat, enhanced glacier mass loss, and ecosystem changes  
52 (Rantanen et al., 2022). Despite numerous studies based on observations and aerosol/climate models (e.g., Bond et al., 2013  
53 and references therein), we have only limited knowledge on BC owing to lack of accurate long-term in situ observations (Mori  
54 et al., 2019). For the Arctic region, data are particularly sparse and few long-term records of BC size distribution exist.

55 Although there have been no direct observations before the past few decades, ice cores drilled in the Arctic have  
56 provided long-term records of BC. Development of the Single-Particle Soot Photometer (hereafter, SP2; Droplet Measurement  
57 Technologies, USA) (Stephens et al., 2003; Baumgardner et al., 2004) enabled measurements of refractory BC (rBC), the

58 [terminology used for incandescence-based BC measurements \(Petzold et al., 2013; Lim et al., 2014\)](#), in Arctic ice cores, where  
59 BC concentrations are low and sample volumes are limited (McConnell et al., 2007; Zdanowicz et al., 2018; Zennaro et al.,  
60 2014; Osmont et al., 2018). A continuous flow analysis (CFA) system is often used with the SP2 for high-resolution analysis  
61 of ice cores (McConnell et al., 2007; Zdanowicz et al., 2018; Zennaro et al., 2014). With an SP2 attached to a CFA system,  
62 McConnell et al. (2007) reconstructed  $\text{rBC}$  mass concentrations in central and southern Greenland since the pre-industrial  
63 period. They showed that  $\text{rBC}$  concentration began a gradual rise after 1850, which was followed by rapid increase around  
64 1890, a peak at around 1910, and then erratic decline through the late 1940s, followed by a sharp drop in the 1950s. They  
65 attributed the increase to  $\text{rBC}$  derived mainly from fossil fuel combustion in North America. Similar anthropogenic temporal  
66 trends have been reported for other Greenland sites (McConnell, 2010). The  $\text{rBC}$  flux records presented by McConnell (2010)  
67 suggest that the anthropogenically derived increase in  $\text{rBC}$  was substantially less in northern Greenland than in southern  
68 Greenland, which is closer to the emission sources in North America and Western Europe. McConnell et al. (2007) also  
69 reported that the greatest increase in anthropogenic  $\text{rBC}$  occurs in winter. However, no  $\text{rBC}$  particle size data from Greenland  
70 ice cores have been published to date.

71 At Arctic sites outside Greenland, only a few ice cores have been analysed for BC. An ice core from Holtedahlfonna  
72 (Svalbard) indicated that BC mass concentration started to increase after 1850 and peaked around 1910, similar to the  $\text{rBC}$   
73 record of ice cores from Greenland (Ruppel et al., 2014). BC concentrations in the Holtedahlfonna core increased again  
74 between 1970 and 2004, reaching unprecedented values in the 1990s. This increase is not seen in Greenland ice cores, and  
75 contradicts atmospheric BC observations from Svalbard and other Arctic sites (Sharma et al., 2013), which indicate declining  
76 concentrations of atmospheric BC. Ruppel et al. (2014) attributed the differences partly to the different sources of  
77 anthropogenic BC affecting Svalbard and Greenland attributable to different air mass trajectories. They also suggested that  
78 changes in scavenging efficiency might have affected the Holtedahlfonna BC record. An ice core from Lomonosovfonna,  
79 another site in Svalbard (Osmont et al., 2018), showed gradual increase in  $\text{rBC}$  during 1800–1859, followed by dramatic  
80 increase from 1860. The concentrations displayed two maxima at around 1870 and 1895, before they started to decline.  
81 Between 1910 and 1949, concentrations of  $\text{rBC}$  were low. In contrast to the concentrations of  $\text{rBC}$  in Greenland, another  
82 notable increase was evident in the Lomonosovfonna core after 1940, and the concentrations were at their highest in the 1950s  
83 and 1960s. The  $\text{rBC}$  concentrations started to decrease in the 1970s, i.e., much later than the start of the decline in Greenland.

84 The authors argued that the differences between Greenland and Lomonosovfonna are partly related to the different source  
85 regions of the air masses reaching Greenland and Svalbard.

86 The differences between the Holtedahlfonna and Lomonosovfonna records might also reflect different methods used  
87 for the measurement of BC mass concentration. The samples from the Holtedahlfonna ice core were filtered, and then the  
88 filters were analysed for BC using a thermal–optical method (Osmont et al., 2018), whereas the Lomonosovfonna and  
89 Greenland ice cores were analysed using an SP2. Uncertainties regarding the filtering efficiency (Ruppel et al., 2014) and the  
90 effects of dust particles on the thermal–optical method could partly explain the differences in the long-term trends in BC  
91 concentrations. Furthermore, melt–freeze cycles that commonly occur at ice coring sites in Svalbard would have affected the  
92 rBC concentrations (Osmont et al., 2018). Moreover, melt–freeze cycles could have agglomerated the rBC particles to larger  
93 sizes beyond the detection range of an ~~an off-the-shelf standard~~ SP2 (Osmont et al., 2018; Wendl et al., 2014). An ice core rBC  
94 record from the Devon Ice Cap in the Canadian Arctic was also found to differ from the records of Greenland ice cores  
95 (Zdanowicz et al., 2018). Although such differences could be partly attributable to different rBC source regions, melt–freeze  
96 cycles could have also affected the Devon Ice Cap record. To investigate whether melt–freeze cycles did affect the derived BC  
97 concentrations, we need to know the sizes of the rBC particles.

98 Even for ice cores drilled at sites where summer melting seldom occurs, such as those from interior Greenland, it is  
99 important to investigate the size distributions of rBC particles to verify whether they are within the detection range of the SP2  
100 instrument. This is because the sizes of rBC particles in snow are often larger than those in the atmosphere (Schwarz et al.,  
101 2013; Mori et al., 2019) and exceed the detection range of a ~~traditional standard~~ SP2, ~~which~~ The upper limit of detectable rBC  
102 diameter is usually ~~between~~ approximately ~~70 and 850~~ 500 nm for the off-the-shelf SP2; that for SP2 modified by Moteki and  
103 Kondo (2010) is approximately 850 nm (Moteki and Kondo, 2010; Mori et al., 2019); and that for the off-the-shelf SP2  
104 Extended Range (SP2-XR) is 800 nm (Mori et al., 2019). If a large proportion of rBC particles have a diameter of >500 nm or  
105 850 nm, the BC mass concentrations would be underestimated (Mori et al., 2019; Goto-Azuma et al., 2024submitted).  
106 Furthermore, if an ultrasonic ~~nebuliser~~ nebulizer, such as the U5000AT (CETAC Technologies, USA), was used with an off-  
107 the-shelf standard SP2, as was the case in most previous studies of rBC in ice cores (McConnell et al., 2007; Kaspari et al.,  
108 2011; Zennaro et al., 2014; Bisiaux et al., 2012a, b; Wang et al., 2015; Zdanowicz et al., 2018; Du et al., 2020), ~~the upper limit~~  
109 ~~of detectable~~ there would be large uncertainties in rBC size would have been <850 nm mass concentrations (Wendl et al., 2014;  
110 Goto-Azuma et al, submitted2024). Because the nebulizing efficiency of this type of nebulizer varies markedly for rBC

111 [particles < 850 nm](#) ~~within this size range~~ (Ohata et al., 2013; Mori et al., 2016; Goto-Azuma et al., 2024), variation in efficiency  
112 should be considered when calculating accurate mass concentrations and size distributions (Ohata et al., 2013). However, this  
113 was not taken into account in most previous ice core studies. It is therefore important to analyse Arctic ice cores using an  
114 instrumental set-up that allows detection of  $rBC$  particles with diameter of  $>850$  nm, and also to consider the size-dependent  
115 efficiency of the nebulizer. We developed a CFA system that includes an  $rBC$  unit, which allows accurate high-resolution  
116 measurement of concentrations and size distributions of  $rBC$  particles with diameter between 70 nm and 4  $\mu$ m. Using this  
117 system, we analysed an ice core drilled at the SIGMA-D site in northwest Greenland. The details of this new system and its  
118 performance are described in the companion paper (Goto-Azuma et al., [2024submitted](#)). In this study, we analysed the data  
119 and investigated the temporal variability in concentration and size distribution of  $rBC$  that originated from fossil fuel  
120 combustion and biomass burning.

121 The BC detected in Arctic ice cores, together with  $NH_4^+$  and specific organic materials (i.e., formate, levoglucosan,  
122 vanillic acid, and p-hydroxybenzoic acid), has been used to reconstruct past biomass burning (Ruppel et al., 2014; Zennaro et  
123 al., 2014; Grieman et al., 2017, 2018; Fischer et al., 2015; Pokhrel et al., 2020; Legrand et al., 2016). Although both BC and  
124  $NH_4^+$  have sources other than biomass burning (Osmont et al., 2018), levoglucosan, vanillic acid, and p-hydroxybenzoic acid  
125 primarily originate from biomass burning. However, the data regarding such organic materials usually have lower temporal  
126 resolution compared with that of  $rBC$  and  $NH_4^+$  data owing to limitations of the measurement techniques. Furthermore, little  
127 is known about their changes during atmospheric transport and post-depositional processes (Hennigan et al., 2010). Different  
128 ice core proxies often show different temporal and spatial trends in biomass burning activities (Legrand and de Angelis, 1996;  
129 Legrand and Mayewski, 1997; Legrand et al., 1992, 2016; Kawamura et al., 2012; Grieman et al., 2017, 2018; Rubino et al.,  
130 2016; Zennaro et al., 2014). Compared with the Global Charcoal Database, which has been used widely to investigate changes  
131 in biomass burning on centennial to orbital time scales (Power et al., 2010; Marlon et al., 2016), ice core proxy records usually  
132 have higher temporal resolution. Even monthly or seasonally resolved continuous records of  $rBC$  and  $NH_4^+$  for the past few  
133 centuries, millennia, and hundred thousand years have been derived from several Arctic ice cores, thereby allowing detection  
134 of high spikes in concentration in summer attributable to large boreal forest fires in northern North America and/or Siberia  
135 (Fischer et al., 2015; Zennaro et al., 2014). However, previous studies using  $rBC$  as a biomass burning tracer have been  
136 restricted to the pre-industrial period. This is because  $rBC$  originated from fossil fuel combustion contributed greatly to the  
137 total  $rBC$  concentrations and obscured the temporal trends in  $rBC$  related to biomass burning.

138 In this study, we reconstructed approximately monthly resolved concentrations and sizes of rBC particles in northwest  
139 Greenland over the past 350 years. The rBC originated both from biomass burning and from fossil fuel combustion was  
140 distinguished owing to their different seasonal variability. In this paper, we discuss the temporal trends in the concentration  
141 and size of rBC particles originated from both sources, and we investigate the rBC source regions based on backward trajectory  
142 analyses. We then estimated the potential albedo reductions based on the monthly mean rBC concentration data.

## 143 2 Materials and Methods

### 144 2.1 Ice core processing, analyses, and dating

145 A 222.7 m ice core was drilled at the SIGMA-D site (77.636° N, 59.120° W; 2100 m a.s.l.; Fig. 1) in northwest Greenland in  
146 spring 2014 (Matoba et al., 2015). The annual mean air temperature and accumulation rate at the site were estimated to be  
147  $-25.6\text{ }^{\circ}\text{C}$  and  $0.23\text{ w eq-yr}^{-1}$ , respectively (Nagatsuka et al., 2021). We examined the melt features (ice layers and thin crusts)  
148 in the uppermost 20 meters of the SIGMA-D ice core, where increased summer melting would be expected due to recent  
149 warming. We observed ice layers, with a maximum thickness of 10 mm, at only three depths. The 20-meter average melt  
150 feature percentage (MFP) was 0.47%. The maximum MFP per meter was 1.7%, and 10 out of the 20 meters had no melt  
151 features. Thus, the effects of melt-refreeze cycles are minimal at the SIGMA-D site.

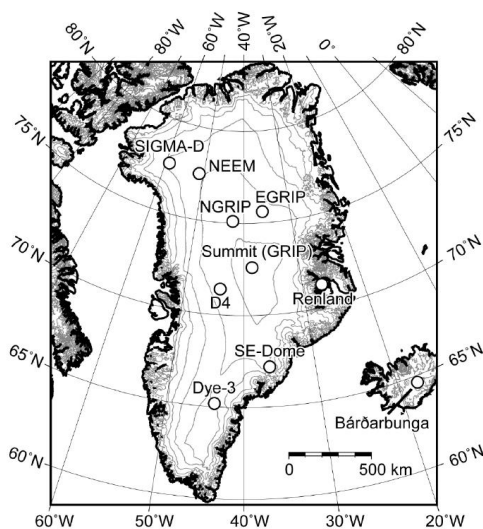


**Figure 1: Location of the SIGMA-D site and that of other drill sites.**

152 The details of the ice core processing and analyses are described in the companion paper (Goto-Azuma et al.,  
153 submitted to Atmospheric Chemistry and Physics 2024); therefore, we provide only a brief summary here. The top 175.77 m

154 of the core was divided into two vertical sections (Sections A and B) in the field. Section A was kept frozen and transported  
155 to the National Institute of Polar Research (NIPR) in Japan; Section B was cut, melted, and bottled in the field.

156

157 Down to the depth of 112.87 m in Section A, we cut quadrangular prism samples with a cross section of 34 mm × 34  
158 mm. For the depth interval between 6.17 and 112.87 m, we analysed rBC, stable ~~isotopes of water isotopes~~, and six elements  
159 (i.e., <sup>23</sup>Na, <sup>24</sup>Mg, <sup>27</sup>Al, <sup>39</sup>K, <sup>40</sup>Ca, and <sup>56</sup>Fe) using the NIPR CFA system. The top 6.17 m of Section A was too fragile to be  
160 analysed using the CFA system; hence, we manually cut it into segments of approximately 0.1 m. These “discrete samples”  
161 were decontaminated in a -20 °C cold room using a precleaned ceramic knife and then placed in powder-free plastic bags.  
162 They were then melted and transferred to precleaned glass and polypropylene bottles in a class 10,000 clean room. The samples  
163 in glass bottles were analysed for stable isotopes of water and rBC. For the discrete samples, stable isotopes of water were  
164 analysed using a near-infrared cavity ring-down spectrometer (L2120-i, Picarro Inc., USA), a high-precision vaporizer (A0211,  
165 Picarro Inc., USA), and an autosampler (PAL HTC9 - xt - LEAP, LEAP Technologies, USA). The precision of determination  
166 was ±0.05‰ for δ<sup>18</sup>O. The samples in the polypropylene bottles were analysed for six elements (i.e., <sup>23</sup>Na, <sup>24</sup>Mg, <sup>27</sup>Al, <sup>39</sup>K,  
167 <sup>40</sup>Ca, and <sup>56</sup>Fe) using an inductively coupled plasma mass spectrometer (7700 ICP-MS, Agilent Technologies, USA) in a class  
168 10,000 clean room at NIPR.

169 Both the CFA samples and the discrete samples were analysed for rBC using a Wide-Range SP2 (Mori et al., 2016),  
170 which is a modified version of the SP2 (Droplet Measurement Technologies, USA), and a concentric pneumatic nebulizer  
171 (Marin-5, Teldyne CETAC, USA). The combination of the Wide-Range SP2 and the pneumatic nebulizer enabled us to extend  
172 the range of the size of rBC particles analysed (70 nm < diameter < 4 μm) to beyond ~~that those~~ of the ~~off-the-shelf standard~~  
173 SP2 (70 nm < diameter < ~~600-850~~500 nm) ~~and the modified SP2 (Moteki and Kondo, 2010) or off-the-shelf SP2-XR (50-70~~  
174 ~~nm < diameter < 800-850 nm)~~. This combination and a careful calibration procedure enabled us to measure not only the  
175 concentration but also the diameter of rBC particles. The analytical errors of the rBC mass and number concentrations were  
176 estimated to be <16% (Mori et al., 2016; [Goto-Azuma et al., 2024](#)). The reproducibility of the rBC number and mass  
177 concentrations for repeated measurements was usually better than 10% (Mori et al., 2019; [Goto-Azuma et al., 2024](#)). The  
178 detection limits of the rBC number and mass concentrations were approximately ~~10-0.35~~ counts·μL<sup>-1</sup> and ~~0.01-0.2~~ μg·L<sup>-1</sup>,  
179 respectively.

180 Depths of Section B above 61.2 m were analysed for Na<sup>+</sup>, K<sup>+</sup>, Mg<sup>2+</sup> ~~and~~, Ca<sup>2+</sup>, Cl<sup>-</sup>, NO<sub>3</sub><sup>-</sup>, and SO<sub>4</sub><sup>2-</sup> using two ion

181 chromatographs (ICS-2100, Thermo Fisher Scientific, USA) at Hokkaido University (Japan), whereas depths between 61.2  
182 and 112.87 m were analysed for  $\text{NH}_4^+$ ,  $\text{Na}^+$ ,  $\text{K}^+$ ,  $\text{Mg}^{2+}$ ,  $\text{Ca}^{2+}$ ,  $\text{Cl}^-$ ,  $\text{NO}_3^-$ , and  $\text{SO}_4^{2-}$  using two ion chromatographs (ICS-2000,  
183 Thermo Fisher Scientific, USA) at NIPR. The limit of detection of  $\text{Na}^+$  measured at Hokkaido University was  $10 \mu\text{g L}^{-1}$ ,  
184 whereas that measured at NIPR was  $0.2 \mu\text{g L}^{-1}$ . Stable ~~water~~ isotopes of water were analysed for all samples from Section B  
185 using a near-infrared cavity ring-down spectrometer (L2130-i, Picarro, USA) and a high-throughput vaporizer (A0212, Picarro,  
186 USA) at Hokkaido University. The precision of determination was  ~~$\pm 0.080$~~   $\pm 0.1$ ‰ for  $\delta^{18}\text{O}$ . For dating purposes, tritium  
187 concentrations were measured using a liquid scintillation counter (LSC-LB3; Aloka Co. Ltd., Japan) at 0.05 m intervals for  
188 the depth interval 19.15–26.47 m (Nagatsuka et al., 2021).

189 Figure 2 shows the seasonal variability in Na and  $\text{Na}^+$  concentrations, together with that in  $\delta^{18}\text{O}$  (~~Goto-Azuma et al.,~~  
190 ~~submitted~~). Concentrations of Na and  $\text{Na}^+$  show maxima in winter and minima in summer, whereas the  $\delta^{18}\text{O}$  shows maxima  
191 in summer and minima in winter (Nagatsuka et al., 2021; Legrand and Mayewski, 1997; Mosher et al., 1993). ~~As reported in~~  
192 ~~the companion paper (Goto-Azuma et al., submitted), w~~ We dated Section B of the SIGMA-D core by annual layer counting  
193 using mainly  $\text{Na}^+$  (Nagatsuka et al., 2021), which exhibited clearer seasonal variation compared to  $\delta^{18}\text{O}$  and other ionic species.  
194 The seasonal variation of  $\delta^{18}\text{O}$ , typically used for annual layer counting, was often obscured by diffusion in the SIGMA-D  
195 core. However, w we supplementarily used  $\text{Ca}^{2+}$  and  $\delta^{18}\text{O}$  data when annual peaks of  $\text{Na}^+$  were not clearly observed.  
196 Additionally, we used a tritium peak (1963) and volcanic  $\text{SO}_4^{2-}$  peaks (Katmai, 1912; Tambora, 1816, unknown, 1810; and  
197 Laki, 1783) as reference horizons, ~~as reported by~~ Nagatsuka et al., (2021). Because the CFA data from Section B and the  
198 discrete data from Section A agreed well (Fig. 2), we basically adopted the chronology of Section B for that of Section A.  
199 ~~However, for the years before 1783, we made with a few~~ minor adjustments ~~where high  $\text{SO}_4^{2-}$  peaks did not match the volcanic~~  
200 ~~eruptions reported from study of other Greenland ice cores (Sigl et al., 2013)~~. The uncertainties of dating were estimated to be  
201 less than  $\pm 2$  years. The CFA data covered 1653–2002 (~~Goto-Azuma et al., submitted~~), and the data from the top 6.17 m covered  
202 the period 2003–2013.

203 We divided one year into 12 months based on the assumption that the annual maxima and minima of  $\text{Na}^+$   
204 concentration correspond to 1 January and 1 July, respectively (Fig. 2). Each depth interval corresponding to a half year was  
205 evenly divided into six months. Using the CFA data, we calculated the annual mean and the monthly mean values of the  
206 number and mass concentrations of rBC particles. It is important to note that the months defined in this study may not align  
207 exactly with calendar months for the following reasons: (1) precipitation is not evenly distributed throughout the year (Figs.



208 A1 and A2); (2) the minima and maxima of Na<sup>+</sup> concentrations do not necessarily coincide with 1 January and 1 July,  
209 respectively; and (3) dry deposition would have a small contribution. As a result, there is inherent uncertainty in this definition.  
210 The discrepancy between the "months" defined in this study and actual calendar months could be one or two months.  
211 Nevertheless, we will refer to these periods as "months" hereafter.

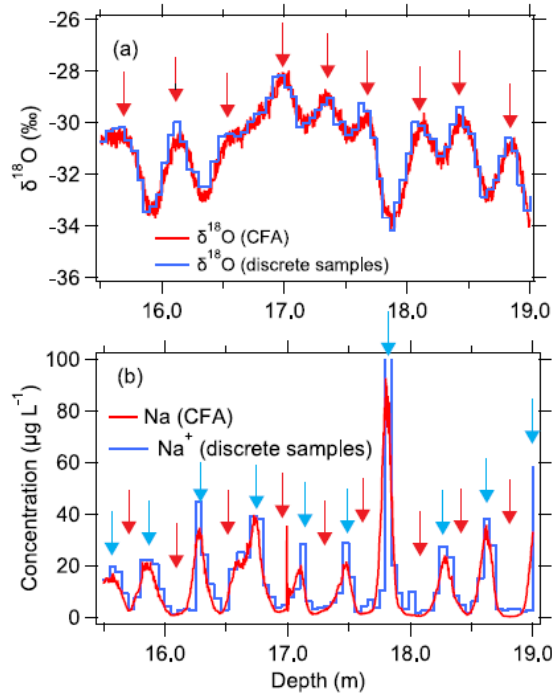


Figure 2: ~~Concentrations of~~(a)  $\delta^{18}\text{O}$  and (b) Na (and  $\text{Na}^+$ ) ~~concentrations~~(Goto-Azuma et al., submitted). Red and blue curves represent data obtained from CFA measurements (this study) and discrete sample measurements (Nagatsuka et al., 2021) of the SIGMA-D core, respectively. Blue and red arrows indicate winter and summer, respectively. Winter and summer peaks were assumed to represent January 1 and July 1 of each year, respectively.

212 As demonstrated in the companion paper (Goto-Azuma et al., 2024), the dispersion lengths of the CFA system are  
213 ~35 and ~39 mm for Na and BC, respectively. However, we could usually resolve two peaks which were 10 mm apart, although  
214 the signal dispersion might slightly reduce the heights of the seasonal peaks.

## 219 2.2 Backward trajectory analysis

220 To estimate the contributions of different air masses affecting the SIGMA-D and D4 sites (Fig. 1), we performed 10-day  
221 backward trajectory analyses for the period 1958–2015. Dividing the globe into 21 regions (Fig. A+A3), we calculated the  
222 contribution from each region. We used the Single-Particle Lagrangian Integrated Trajectory (HySPLIT) model developed by  
223 the National Oceanographic and Atmospheric Administration (NOAA) (Stein et al., 2015). The initial air mass was set at three  
224 elevations at each site (i.e., 500, 1000, and 1500 m above ground level), and the accumulated probability of the air mass in  
225 each 1° grid cell was calculated. Assuming wet deposition of rBC at the ice core sites, the air mass probability was weighted  
226 with the local daily precipitation, i.e., if no precipitation occurred, the air mass was not considered, and vice versa. We used  
227 ERA5 precipitation data produced by the European Centre for Medium-Range Weather Forecasts (Hersbach et al., 2020).  
228 Details of the procedures are described in previous studies (Parvin et al., 2019; Nagatsuka et al., 2021; Nagatsuka et al., 2023).  
229 For comparison, we also calculated the regional contributions without weighted for precipitation, while accounting for dry  
230 deposition. However, we anticipate that dry deposition contributes only minimally compared to wet deposition (Appendix B).

231

### 232 3 Results and Discussion

#### 233 3.1 Impacts of anthropogenic emissions on long-term trends in concentrations and sizes of rBC particles

234 Figure 3 displays annual and decadal averages of number and mass concentrations of rBC during the past 350 years. Notably,  
235 monthly mean values could have been affected by the values of the adjacent few one-two months, considering the resolution  
236 of the CFA data (10–40 mm) estimated from signal dispersion tests (Sect. 2.1 and Goto-Azuma et al., submitted2024). Because

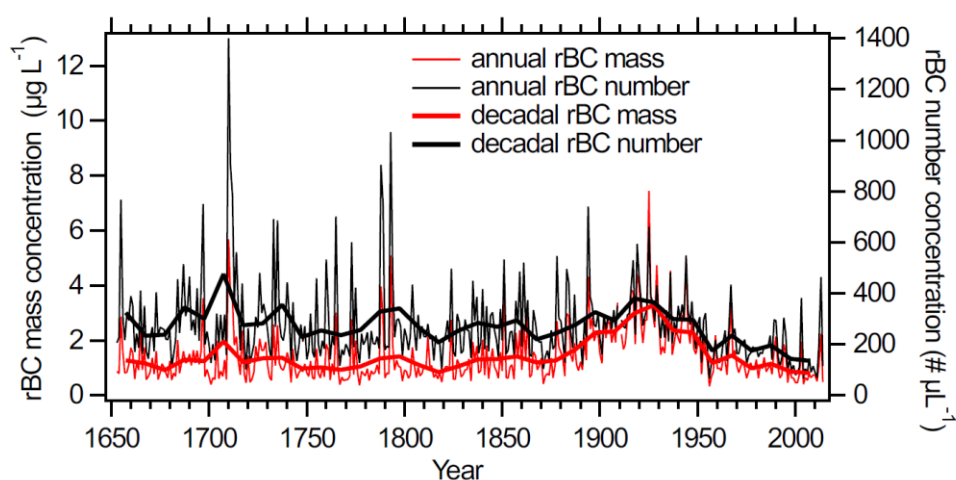


**Figure 3: Annual mean (thin curves) and decadal mean (thick curves) concentrations of rBC. Red and black curves represent mass and number concentrations, respectively.**

237 we melted the core from the bottom to the top, the data for ~~a few~~one-two months after large rBC concentration peaks could  
238 have been affected. However, the annual and decadal averages were unaffected by the CFA signal dispersion. We have also  
239 calculated annual rBC mass flux using annual mean rBC mass concentration data and annual accumulation rate data (Fig.A4).  
240 Since there are no long-term trends in annual accumulation rates, the temporal trends in rBC mass concentrations and  
241 rBC mass fluxes are consistent. Therefore, we used concentration data in the following discussion.

242 Many of the very high mass and number concentration peaks such as those in 1710 originated from large boreal forest  
243 fires, as discussed in Sect. 3.3. Apart from these sporadic sharp peaks in number and mass concentrations, their background  
244 levels started to increase in the 1870s, reached their maxima in the 1910s–1920s, and decreased again ~~after~~since the 1930s.  
245 Breakpoint analysis (Muggeo, 2003; de la Casa and Nasello, 2010) confirmed the timing of these increases and decreases. In  
246 the 1960s, rBC number and mass concentrations returned to their pre-industrial levels. In the 1980s and 1990s, number  
247 concentrations were below the pre-industrial level, whereas mass concentrations were similar to those of the pre-industrial  
248 level. Before 1850, the major sources of rBC in Greenland were likely to have been biomass burning emissions from boreal  
249 forest fires (Legrand et al., 2016; McConnell et al., 2007; Zennaro et al., 2014). The increases in rBC concentrations that  
250 occurred in the late 19<sup>th</sup> century to mid-20<sup>th</sup> century are likely attributable to inflow to Greenland of rBC of anthropogenic  
251 origin, as reported previously (McConnell, 2010; McConnell et al., 2007). \_

252  
253 Direct comparison between the rBC concentrations in the SIGMA-D core and those in other Greenland ice cores is  
254 not strictly feasible owing to methodological differences. rBC measurements in other Greenland ice cores were conducted  
255 using the ~~standard-off-the-shelf~~ SP2 coupled with an ultrasonic nebulizer (McConnell et al., 2007; McConnell, 2010; Zennaro  
256 et al., 2014). This setup allows for the measurement of rBC particles with diameter of less than ~~600~~500–650 nm (Goto-Azuma  
257 et al., submitted2024). In contrast, the measurements of the SIGMA-D ice core could detect rBC particles with diameter up to  
258 4  $\mu\text{m}$ . Therefore, rBC concentrations in other Greenland ice cores might have been underestimated during periods when the  
259 diameter of large proportions of rBC particles exceeded approximately ~~650~~500 nm. Owing to lack of information on size  
260 distributions, the extent of the underestimation for other Greenland ice cores remains unknown. As described in the companion  
261 paper (Goto-Azuma et al., submitted2024), if the ~~measurement method~~off-the-shelf SP2 used in the previous studies had also  
262 been used for the SIGMA-D ice core, the extent of underestimation would have depended on depth and hence on age. However,  
263 the general temporal trends in annual mean rBC concentrations at the SIGMA-D site did not change notably if rBC particles

264 with diameter of  $>650-500$  nm, the maximum measurable diameter of the off-the-shelf SP2, were excluded (Fig. 4). Therefore,  
265 it is informative to compare the  $rBC$  concentration trends at the SIGMA-D site with those of other Greenland sites.  
266

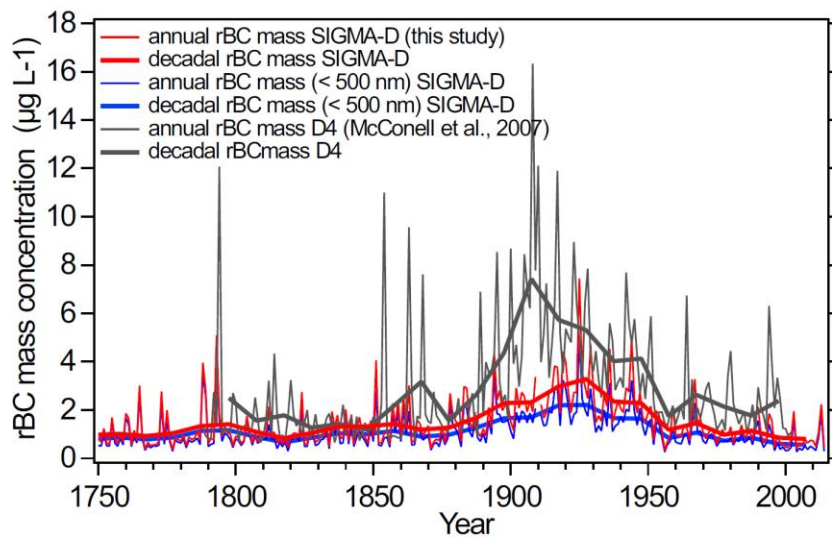


**Figure 4: Annual mean (thin curves) and decadal mean (thick curves) mass concentrations of  $rBC$ . Red and black curves represent  $rBC$  concentrations at the SIGMA-D and D4 sites, respectively. Blue curves show annual  $rBC$  concentrations for  $rBC$  particles with diameter of  $<650-500$  nm.**

267  
268 The long-term trends in  $rBC$  mass concentrations at the SIGMA-D site are broadly similar to those at other ice core  
269 sites in Greenland (McConnell et al., 2007; McConnel., 2010), including the D4 site. However, the SIGMA-D core shows  
270 much lower anthropogenic  $rBC$  concentrations, a later peak period, and later onset of the reductions in comparison with those  
271 of the D4 core (Fig. 4). This is in accord with the studies by McConnel et al. (2007) and McConnel (2010), which indicate that  
272 more southerly sites generally show higher anthropogenic  $rBC$  concentrations, an earlier peak period, and earlier onset of the  
273 decline in anthropogenic  $rBC$  concentrations in comparison with those of more northerly sites. The BC emission inventories  
274 for potential BC source regions indicate that emissions of anthropogenically derived BC started earlier in Europe than in North  
275 America, and that the decline in anthropogenic BC concentrations started earlier in North America than in Europe or the former  
276 USSR (Osmont et al., 2018). The emission inventories used by Osmont et al. (2018) were those adopted for the Coupled Model  
277 Intercomparison Project phase 5 (CMIP 5; Bauer et al., 2013; Eckhardt et al., 2023; Lamarque et al., 2010). If those emission

278 inventories are reliable, then the slight difference in the temporal trends of  $r_{BC}$  concentrations would indicate that southern  
279 Greenland sites (e.g., the D4 site) had been influenced mainly by anthropogenic emissions from North America, whereas  
280 northern Greenland sites (e.g., the SIGMA-D site) had been influenced by anthropogenic emissions from Europe and the  
281 former USSR (in addition to those from North America), as was the case for anthropogenic sulphate (Goto-Azuma and Koerner,  
282 2001). However, the results of our backward trajectory study do not support this hypothesis, as discussed below.

283 The 10-day precipitation-weighted backward trajectories for the SIGMA-D and D4 sites showed no contributions of  
284 air masses from Antarctica (AT), Australia and New Zealand (AUS), South America (SAM), Southeast Asia (SEA), South  
285 Asia (SA), the Antarctic Ocean (ATO), South Pacific Ocean (SPO), Indian Ocean (INO), and South Atlantic Ocean (SAO).  
286 The four regions of the Middle East (ME), Africa (AF), East Asia (EA), and Central Asia (CA) (Fig. 5) showed maximum  
287 contributions of <0.05%. In further analyses, we omitted the above 13 regions and focused on the eight regions of Europe  
288 (EU), the Greenland Ice sheet (GrIS), Russia (RUS), North America (NA), the North Pacific Ocean (NPO), North Atlantic  
289 Ocean (NAO), Arctic Ocean (AO), and Iceland (IC) (Fig. 5). Of these, GrIS, AO, NA, and NAO were found to be the major  
290 sources of the air masses arriving at both the SIGMA-D site and the D4 site, although only NA represents a source of  
291 anthropogenic BC emissions. Therefore, the temporal trends in anthropogenic  $r_{BC}$  at both SIGMA-D and D4 appear to reflect  
292 the trend of BC emission in NA.

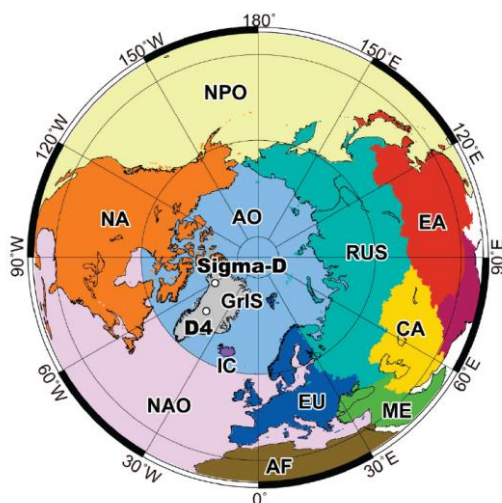


Figure 5: The 12 regions used showing non-zero contributions in for precipitation-weighted backward trajectory analyses (GrIS: Greenland Ice Sheet, NA: North America, EU: Europe, RUS: Russia, CA: Central Asia, EA: East Asia, ME: Middle East, AF: Africa, NPO: North Pacific Ocean, NAO: North Atlantic Ocean, AO: Arctic Ocean, and IC: Iceland).

293 For precipitation-weighted trajectories, The contributions of air masses from EU and RUS, which are regions with  
294 high levels of emission of anthropogenic BC (Hoesly et al., 2018), were less than 4% and 1%, respectively, at both the SIGMA-  
295 D site and the D4 site, even in winter.

296 when their contributions are at their maxima. To investigate the influence of contributions from EU and RUS in more  
297 detail, we recalculated the air mass contributions by excluding GrIS and the oceanic regions of NPO, NAO, and AO where  
298 there are no sources of BC emission. Although GrIS had the largest air mass contributions throughout the year and throughout  
299 the 10 days, we excluded it because most of the region is covered with ice and has very minor BC sources. The temporal  
300 variations in the contributions from NA, EU, RUS, and IC are plotted in Fig. 6 (for both precipitation-weighted and unweighted  
301 trajectories), and the probability distributions of the air masses for the SIGMA-D and D4 sites are displayed in Fig. 7 (for  
302 precipitation-weighted trajectories) and Fig. A5 (for precipitation-unweighted trajectories). ~~In winter, when~~ Except for the  
303 initial few days at D4, the anthropogenic input of BC is greatest at both the SIGMA-D site (see Sect 3.2) and the D4 site  
304 (McConnell et al., 2007), contributions from NA are the highest at both SIGMA-D and D4 sites for both precipitation-weighted  
305 and unweighted trajectories throughout the year. The significant contributions of IC during the first few days at the D4 site are  
306 likely due to its proximity to Greenland despite its small area, since IC is the only land region near Greenland that can  
307 serve as a BC source region. However, if we include oceanic regions along with land regions, the contribution from IC  
308 decreases substantially.

309 At both SIGMA-D and D4 sites, the contributions from EU and RUS increase in winter (Figs. 6, ~~and 7, and A5~~) when  
310 air masses from distant sources can more easily reach the Arctic (Jurányi et al., 2023) for both precipitation-weighted and  
311 unweighted trajectories. Against our expectation based on CMIP 5 emission inventories, the contributions from EU were  
312 slightly greater at D4 than at SIGMA-D. ~~The contributions from RUS were similar at both sites and comprised approximately~~  
313 ~~20% of the total at most.~~ Although backward trajectory analyses showed that contributions from EU were slightly different  
314 between the SIGMA-D and D4 sites, the results suggested the opposite conclusion to that of an assumption based on the  
315 regional difference in emission inventories to explain the slight differences in the temporal trend of rBC at the two sites. For  
316 precipitation-weighted trajectories, the contributions from RUS were similar at both sites and comprised approximately 5% of  
317 the total at most in winter, when the anthropogenic input of rBC is greatest at both the SIGMA-D site (see Sect 3.2) and the  
318 D4 site (McConnell et al., 2007). While precipitation-unweighted trajectories in winter show higher contribution from RUS  
319 compared with precipitation-weighted trajectories at both SIGMA-D and D4 sites, the contribution from RUS is greater at the

320 SIGMA-D site than at the D4 site. The slight difference in temporal patterns of mass concentrations of anthropogenic rBC  
 321 between the two sites might reflect the different contributions from RUS in winter. However, it should be noted that the 1958-  
 322 2015 timeframe used for back trajectory calculations, a constraint given by availability of reanalysis data, is not  
 323 necessarily representative of the entire 350-year period. Nagatsuka et al. (2021), based on the back trajectory studies for  
 324 the SIGMA-D site, have shown that the interannual variability of contributions from different regions remained relatively  
 325 constant during 1958-2013. Thus, we can discuss the source regions of rBC for this period based on our back trajectory  
 326 calculations. For earlier periods, we can only hypothesize the back trajectories by assuming similar atmospheric  
 327 circulations to those of the 1958-2015 period. This could lead to large uncertainties for the years before 1958.  
 328

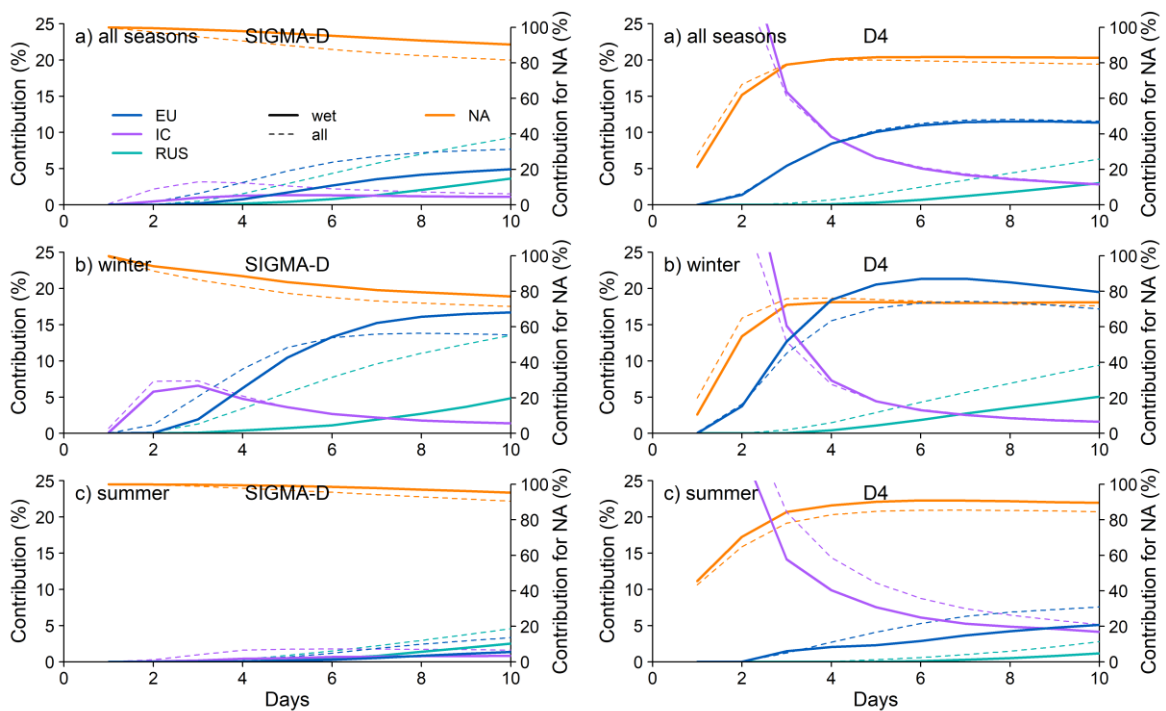


**Figure 6:** Temporal variability in contribution of air masses arriving at (left) the SIGMA-D site and (right) the D4 site from four regions: (a) averages of 12 months, (b) averages of winter months (December-February), and (c) averages of summer months (May-July). Right-hand axes indicate contributions from NA, and left-hand axes indicate contributions from the other regions. Solid and dashed curves denote results with and without weighing for the daily local precipitation, respectively.

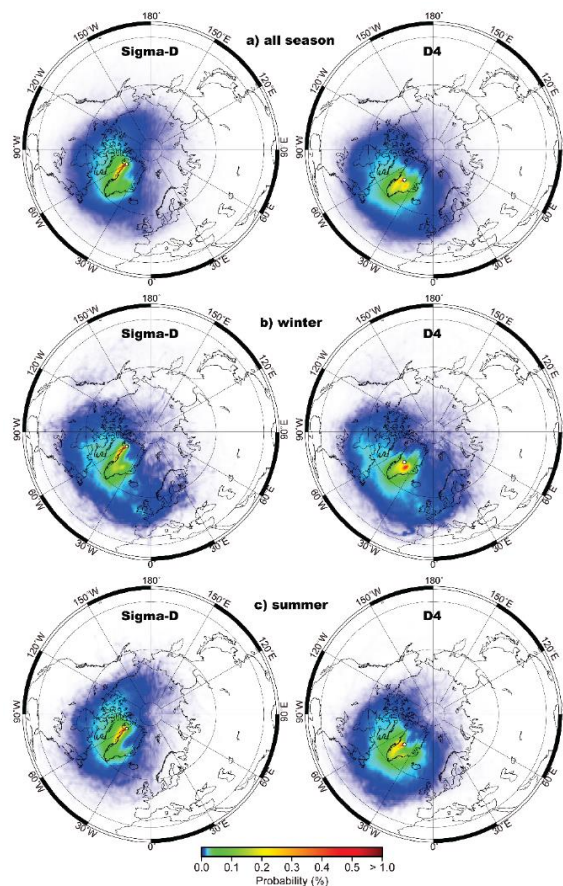


**Figure 7: Probability distributions of air masses at (left) the SIGMA-D site and (right) the D4 site: (a) averages of all seasons, (b) averages of winter months (December–February), and (c) averages of summer months (May–July).**

329 Notably Additionally, there are large uncertainties in emission inventories. Although the CMIP 5 emission inventories  
 330 appear to reproduce the temporal patterns in concentrations and fluxes of  $r_{BC}$  in Arctic ice cores better than those produced  
 331 using the Coupled Model Intercomparison Project phase 6 (CMIP 6) inventories, the reproduction of the magnitudes of the  
 332 concentrations and fluxes is better when using the CMIP 6 inventories (Eckhardt et al., 2023). A model intercomparison study,  
 333 which compared the modelling results obtained from 11 Earth System Models using CMIP 6 emission inventories with  $r_{BC}$   
 334 records from ice cores (Moseid et al., 2022), revealed errors in European emission inventories. However, the study also showed  
 335 that  $r_{BC}$  concentrations in Northern Greenland ice cores reflected European emissions, contradicting our backward trajectory  
 336 analyses. It should be also noted that backward trajectory analyses are unable to capture the contributions of air masses  
 337 transported through the upper troposphere (Nagatsuka et al., 2021), which could be important when estimating the  
 338 contributions from distant sources. Currently, we are unable to explain the slightly different temporal trends in the  $r_{BC}$  records  
 339 from different ice cores in Greenland. Further elucidation of this topic will require additional modelling studies constrained by  
 340 accurate  $r_{BC}$  records from Greenland ice cores.



341 Figure 8 displays decadal mean mass and number size distributions of  $rBC$  for different periods with different  
 342 anthropogenic inputs. We assumed that the mass size distribution follows a Gaussian-lognormal distribution and thus we  
 343 estimated the mass median diameter (MMD), which is one of the measures of an  $rBC$  size distribution. The decadal mean  
 344 MMD was 226 nm in the pre-industrial period of 1783–1792. It increased to 325 nm in the peak anthropogenic period of 1913–  
 345 1922, and subsequently decreased to 302 nm in 1993–2002 and 278 nm in 2003–2012. Number size distributions did not show  
 346 noticeable temporal change. To investigate the temporal changes in  $rBC$  size distribution, we used the average mass of  $rBC$   
 347 particles (mBC) in addition to the MMD. The parameter mBC can be calculated by dividing the mass concentration by the  
 348 number concentration. Figure 9 shows the annual and decadal mean mBC and decadal mean MMD, together with the annual  
 349 and decadal mean  $rBC$  mass concentrations. ~~Of the two size parameters, mBC is easier to calculate than MMD; hence, it can~~  
 350 ~~be used to investigate changes with high temporal resolution. Based on breakpoint analyses, we deduced the timing of  $rBC$~~

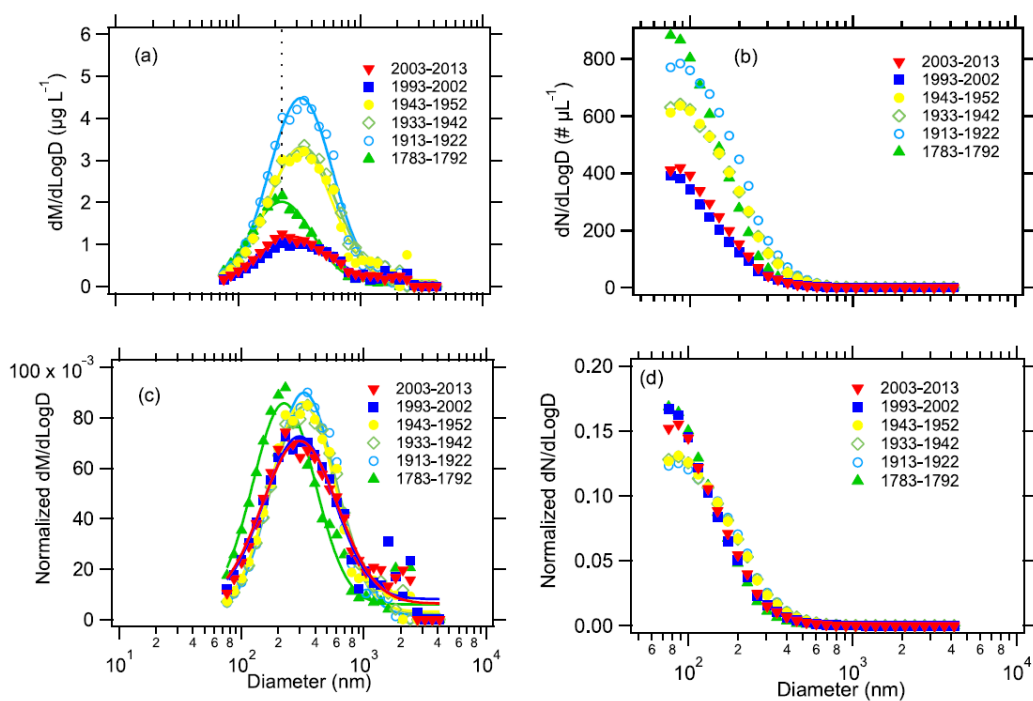


**Figure 8: Temporal changes in decadal mean size distributions of  $rBC$  particles: (a) and (b) non-normalized mass and number size distributions, respectively, and (c) and (d) ~~normalized~~ mass and number size distributions normalized by total  $rBC$  mass and number concentrations, respectively. Dotted line in (a) indicates the mass median diameter (MMD) for the period 1783–1792.**

351 ~~size changes. Both the~~The annual mean mBC and decadal mean mBC started to increase in the 1850s and the 1840s,

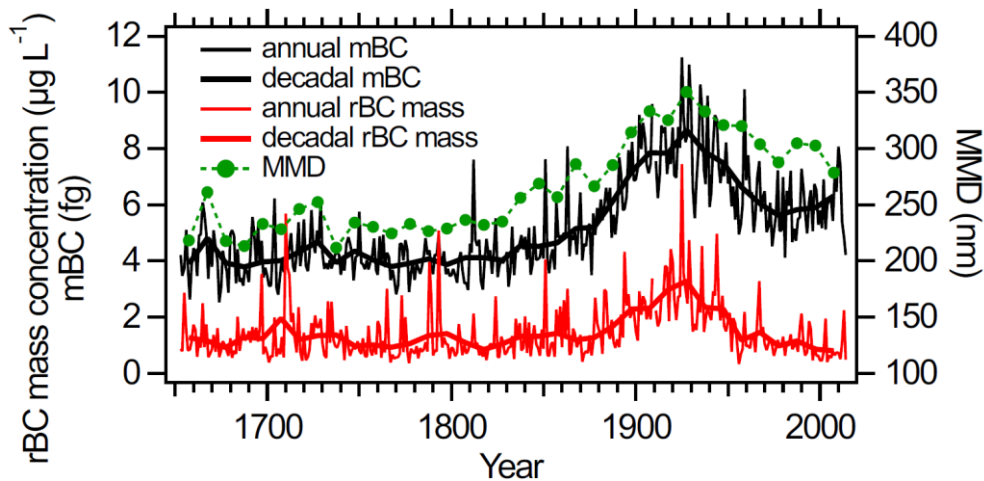
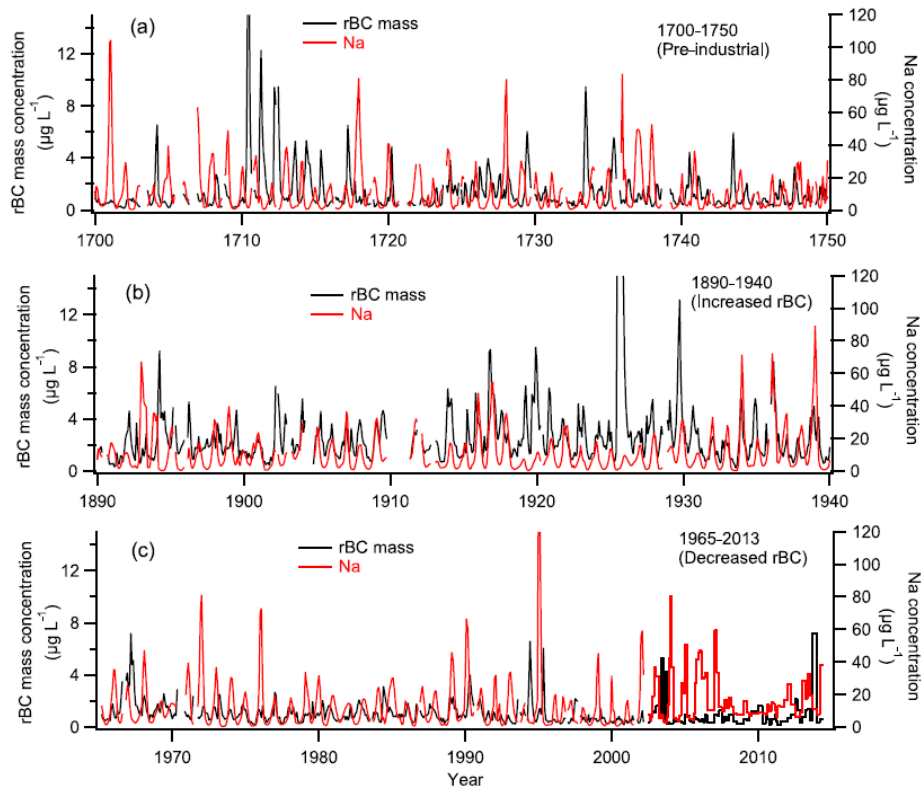


Figure 9: Annual and decadal mean mBC (black) and decadal mean MMD (green), together with annual and decadal mean rBC mass concentration (red). Thin and thick solid lines denote annual and decadal means, respectively.

respectively, while the decadal mean MMD started to increase in the 1820s. Annual mean mBC, decadal mean mBC, and decadal mean MMD and peaked in the 1910s–1920s, when the mass and number concentrations of rBC were at their maxima. The peak values of MMD and mBC were approximately twice and 1.5 times, as high as the corresponding pre-industrial values, respectively. Anthropogenically derived rBC particles that arrived in northwest Greenland appear to have been larger than rBC particles of biomass burning origin. This is contrary to our expectation because it has been reported that the sizes of rBC particles from biomass burning are larger than those from anthropogenic emissions near the sources (Bond et al., 2013). In the 1920s or 1930s, MMD and mBC both started to decrease, as did the mass and number concentrations of rBC particles. However, in contrast to rBC concentrations, neither MMD nor mBC returned to their pre-industrial levels; instead, they remained approximately 1.3 and 1.5 times higher than their pre-industrial levels, respectively. We also notice that the start of the increases in mBC and MMD appear to have occurred earlier than the increases in mass and number concentrations of rBC by 30–40 years.

### 3.2 Temporal changes in seasonal variations in concentrations and sizes of rBC particles

Figure 10 compares the monthly mean rBC mass concentrations in three periods: the pre-industrial period, the period with high anthropogenic input, and recent years when concentrations decreased and returned to pre-industrial levels. Changes are



**Figure 10: Monthly mean  $\underline{rBC}$  mass concentrations and Na concentrations in three periods calculated from the CFA data, with the exception of 2003–2013 (concentrations for this period are raw data from the discrete samples that were analysed with monthly–bimonthly resolution).**

367 evident in the seasonality of  $\underline{rBC}$  concentrations with respect to Na concentrations, which peak in winter. As reported by  
 368 McConnell et al. (2007) in relation to the D4 core,  $\underline{rBC}$  concentrations peaked in summer in the pre-industrial period, whereas  
 369 they peaked in late-winter to early spring during the peak industrial period. Figure 10 also indicates that in recent years after  
 370 the  $\underline{rBC}$  concentrations returned to their pre-industrial levels, the peaks once again occurred in summer. During the transition  
 371 period between the pre-industrial and the peak anthropogenic periods, and that between the peak anthropogenic period and  
 372 recent years, concentrations show complex seasonal variability. For example, in some years, peaks occurred in both summer  
 373 and winter/early spring, whereas seasonal peaks were obscured or summer peaks and winter/early spring peaks appeared  
 374 alternately in other years.

375

376 To examine the general temporal trends in seasonal variations in  $\underline{rBC}$  mass concentrations, we plotted 20-year  
 377 averages of  $\underline{rBC}$  mass concentrations in each month for the years 1653–1992 and we plotted 10-year averages for 1993–2002

378 (Fig. 11). Up until the 20-year period of 1853–1872,  $\underline{r}$ BC mass concentrations were elevated from March to September, peaking  
 379 in the late-spring to summer months (i.e., May–July). After the 20-year period of 1853–1872,  $\underline{r}$ BC concentrations in autumn  
 380 to spring increased and became dominant. During the first half of the 20<sup>th</sup> century,  $\underline{r}$ BC mass concentrations peaked in the  
 381 winter months of December and January. The autumn to spring increases in  $\underline{r}$ BC concentrations are likely attributable to inflow  
 382 of anthropogenic emissions (McConnell et al., 2007). The seasonality of the anthropogenic  $\underline{r}$ BC at SIGMA-D is consistent  
 383 with that of the present-day atmospheric  $\underline{r}$ BC observations at Arctic sites such as Alert (Canadian high Arctic), Ny-Alesund  
 384 (Svalbard), Barrow (Alaska), and a Greenland coastal site (Sharma et al., 2006, 2019; Gong et al., 2010; Qi and Wang, 2019;

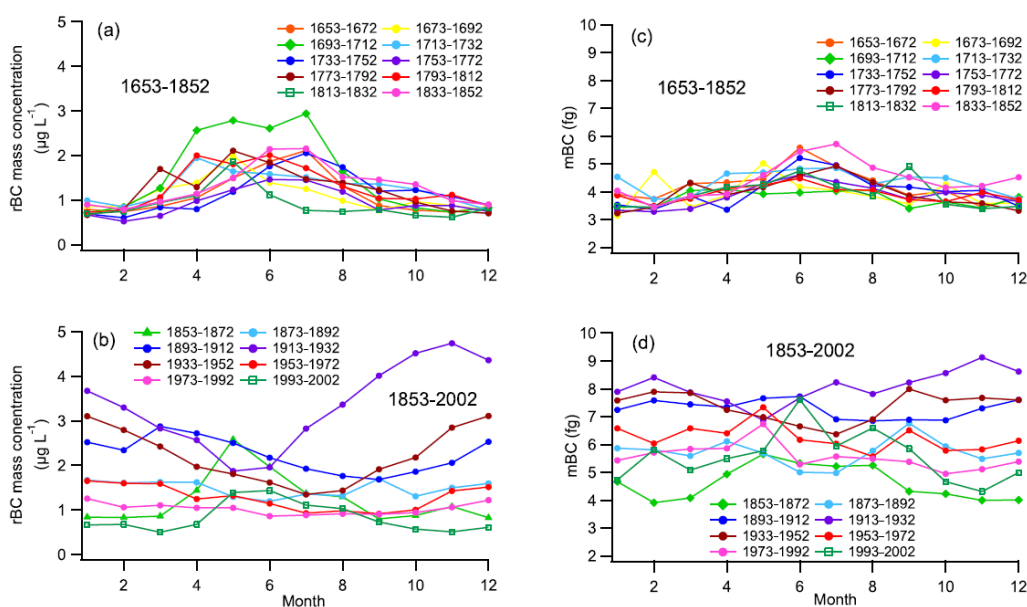


**Figure 11: Twenty-year averages of (a) and (b)  $\underline{r}$ BC mass concentrations and (c) and (d) mBC in each month for the years 1653–1992 and the 10-year averages for 1993–2002.**

385 Massling et al., 2015).

386

387 After the 20-year period of 1913–1933, when the anthropogenic input was at its maximum, the autumn to spring  
 388 concentrations decreased. During 1993–2002, the  $\underline{r}$ BC mass concentration peaked in summer again. The recent seasonality of  
 389  $\underline{r}$ BC at the SIGMA-D site is the same as that observed at other Greenland ice-coring sites, including EGRIP (Du et al., 2020)  
 390 and Summit (Fig. 1) (Schmeisser et al., 2018), but it differs from that of atmospheric observations in the Arctic (including  
 391 Greenland), where  $\underline{r}$ BC concentrations peak in winter/early spring (Sharma et al., 2006, 2019; Gong et al., 2010; Qi and Wang,

2019; Massling et al., 2015). Although we do not present the results for  $rBC$  number concentrations, they showed seasonal variations similar to those found in mass concentrations. The influence of anthropogenic emissions in the recent two decades appears to be much lower at the ice coring sites of SIGMA-D, EGRIP, and Summit, located at elevations of  $>2000$  m a.s.l., in comparison with that at atmospheric observation sites located near sea level where anthropogenic emissions remain dominant. At the high-elevation sites on the GrIS, concentrations of  $rBC$  from biomass burning have exceeded those associated with anthropogenic emissions since the late 20<sup>th</sup> century, which is likely attributable to reduced emissions of anthropogenically derived  $rBC$ , primarily in NA and secondarily in EU (McConnell, 2010; McConnell et al., 2007; Moseid et al., 2022).

To understand the general temporal trends in seasonal variations in  $rBC$  size, we plotted 20-year averages of  $mBC$  in each month for the years of 1653–1992 and we plotted 10-year averages for 1993–2002 (Fig. 11). Up until the 20-year period of 1853–1872,  $mBC$  peaked in spring to the summer months (May–July) in most of the 20-year periods and it never peaked in the winter months. After the 20-year period of ~~1873–1853–1892–1872~~,  $mBC$  in autumn–spring increased, and its seasonality became obscured. After the peak anthropogenic period of 1913–1933,  $mBC$  in autumn–spring decreased. During 1993–2002,  $mBC$  once again peaked in summer. We see similar temporal trends in Figs. 12 and 13, i.e., both MMD and  $mBC$  showed higher values in summer in the pre-industrial period. This seasonality would indicate that the sizes of  $rBC$  particles originated from biomass burning are greater in summer than in winter. The winter and summer ~~values- $mBC$~~  started to increase in the ~~1830s–1820s–1840s–1830s~~ with a larger rates of increase for winter ~~values- $mBC$~~ . Winter and summer values both peaked in the ~~1910s–1890s–19430s~~ and subsequently decreased, with ~~similar-a larger rates of decrease for winter-and-summer~~. ~~The winter and summer MMD started to increase in the 1840s and 1810s, respectively, with larger rate of increase for winter MMD. While winter MMD started to decrease in the 1900s – 1920s and has continued to decrease, the summer MMD did not exhibit a clear downward trend.~~ During the peak anthropogenic period, the summer and winter ~~values- $mBC$  and MMD~~ were close, which obscured the seasonality in  $rBC$  particle size (Fig. 11(b)). ~~We also note that during the peak anthropogenic period,  $rBC$  particles larger than 1  $\mu\text{m}$  in diameter increased in winter (Fig. 13).~~ The winter values of MMD and  $mBC$  became lower than the summer values in 1993–2002. Larger  $rBC$  particles in winter in the anthropogenic period support the argument that  $rBC$  particles deposited at SIGMA-D were larger when originating from anthropogenic emissions than when associated with biomass burning.

In the pre-industrial period, biomass burning would have been the predominant source of  $rBC$ . Backward trajectory analyses (Figs. 6 ~~and~~ 7, and A5) indicate that boreal forest fires in NA would be the primary sources of  $rBC$  in summer at

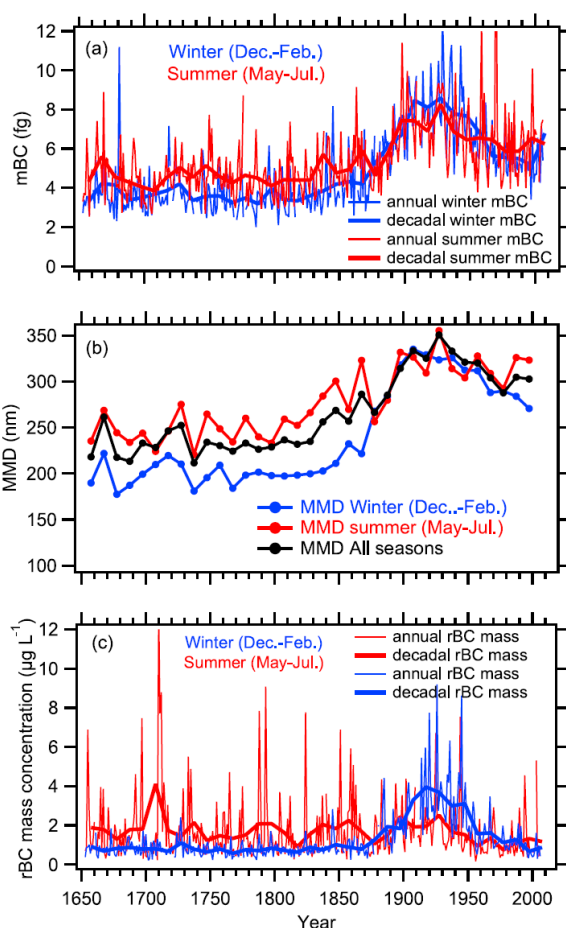


**Figure 12: (a) Annual and decadal means of winter (December–February) and summer (May–July) mBC, (b) decadal means of winter, summer, and all-season (January–December) MMD, and (c) annual and decadal means of winter and summer rBC mass concentrations. In all panels, thin and thick solid lines denote annual and decadal means, respectively. Blue, red, and black curves denote winter, summer, and all-season means, respectively.**

419 both the SIGMA-D site and the D4 site. Although the contributions of air masses from RUS are very small, especially in  
 420 summer (<3% at SIGMA-D; <1% at D4 [for precipitation-weighted trajectories](#)), Siberia has also been proposed as a potential  
 421 source of pyrogenic aerosols to Greenland (Zennaro et al., 2014). A recent study using the CAM-ATRAS global climate–  
 422 aerosol model (Matsui et al., 2022) showed that Siberia has made the largest contribution to rBC concentrations found in the  
 423 recent Arctic snow, although the contribution to Greenland snow specifically has not been reported. ~~We speculate that biomass~~  
 424 ~~burning in~~Therefore, Siberia could be a secondary source of rBC at the SIGMA-D site in summer ~~because the backward~~  
 425 ~~trajectory analyses showed that air masses originated from Siberia (Fig. 7)~~. In winter, the boreal forests in NA and Siberia are  
 426 covered with snow and thus there is little contribution of BC from boreal forest fires (Bond et al., 2013). However, rBC

427 concentrations are not zero, even in winter. Biomass burning in lower latitudes (Zennaro et al., 2014) could be a source of  $rBC$   
428 in winter, and the smaller sizes of  $rBC$  particles in pre-industrial winter periods suggest long-range transport of  $rBC$  that  
429 supports this assumption.

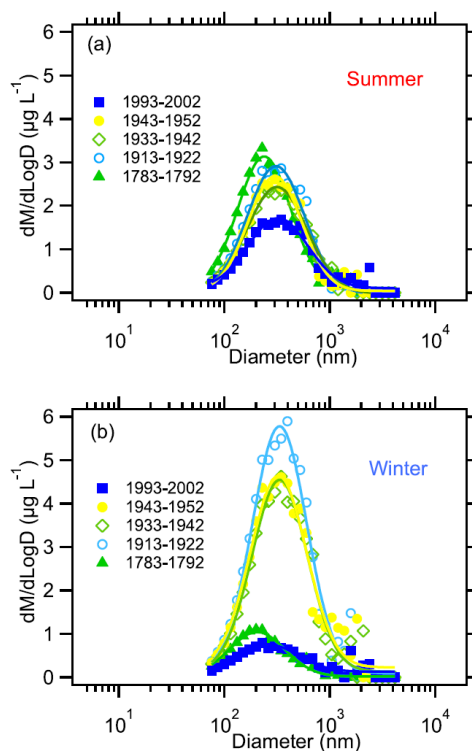


**Figure 13: Temporal variability in mass size distributions of  $rBC$  particles during (a) winter (December–February) and (b) summer (May–July).**

### 430 431 3.3 Historical changes in $rBC$ originated from biomass burning

432 Figure 13–14 presents monthly mean  $rBC$  mass concentrations for the past 350 years, together with  $\text{NH}_4^+$  concentrations.  
433 Occasional high peaks in summer, which lasted for one-two months, likely originated from large boreal forest fires, mainly in  
434 NA but with possible additional contributions from Siberia. Many of the high  $rBC$  peaks in summer coincide with high  $\text{NH}_4^+$   
435 concentration peaks in summer, which originate from large boreal forest fires (e.g., Legrand et al., 2016). Table A1 lists the  
436 biomass burning events distinguished in the record of the SIGMA-D ice core, and in other ice cores and the surface snow of  
437 Greenland. The events distinguished in the SIGMA-D core were defined using  $rBC$  mass concentration peaks and  $\text{NH}_4^+$   
438 concentration peaks. For  $rBC$ , peaks exceeding the summer (May–July) averages for 350 years +  $2\sigma$  or  $3\sigma$  were selected,  
439 whereas for  $\text{NH}_4^+$ , summer peaks exceeding the annual averages for 350 years +  $2\sigma$  or  $3\sigma$  were selected. If an  $rBC$  or  $\text{NH}_4^+$

440 summer peak in the SIGMA-D core with a concentration between the average + 1 $\sigma$  and 2 $\sigma$  was found in the same year as when  
441 a large biomass burning event was recorded at other Greenland sites, we also selected that peak as a biomass burning event. If  
442 the year of a biomass burning event reported by previous studies agreed with that in the SIGMA-D core to within  $\pm 2$  years,  
443 taking account of dating errors in different ice cores, we assumed that the record in the different cores reflected the same event.  
444 In Fig. ~~13~~14(b), we marked only those events exceeding the average + 3 $\sigma$ . Most of the marked events (peaks in 1655, 1665,  
445 1697, 1710, 1711, 1712, 1733, 1788, 1793, 1824, 1851, 1859, 1863, 1925, and 1944) occurred in May, June, or July; however,  
446 those in 1789, 1812, and 1894 occurred in April, the one in 1773 occurred in September, and the one in 1929 occurred in  
447 ~~August~~September-October. The peaks in 1925 occurred in July-August, and that in 1944 occurred in May and June, and we  
448 assumed that they originated from large biomass burning events. Nevertheless, we could not abandon the possibility that these  
449 summer peaks might have been affected by large peaks in the preceding winters owing to signal dispersion in the CFA system.

450 Most of the large events with  $\underline{r}BC$  concentrations that exceeded the average + 3 $\sigma$  were also recorded in boreal forest  
451 fire records reconstructed from  $\underline{r}BC$ ,  $NH_4^+$ , or levoglucosan concentrations in other Greenland ice cores (Table A1). The high  
452  $\underline{r}BC$  concentration peaks in the summers of 1665, 1710, 1711, 1712, 1812, and 1824, accompanying high  $NH_4^+$  peaks, and the  
453 high  $\underline{r}BC$  peak in 1859 have not been reported previously. The high  $NH_4^+$  concentration peaks in 1675, 1690, and 1750 have  
454 no corresponding  $\underline{r}BC$  peaks in April, May, June, July, or August, while those in ~~1675~~1697, 1710, 1712, 1715, and 1761 do  
455 have corresponding  $\underline{r}BC$  peaks. As for the  $NH_4^+$  concentration peak in 1690, the summer  $\underline{r}BC$  data were missing and therefore  
456 comparison was not possible. Although Keegan et al. (2014) argued that the high summer  $\underline{r}BC$  concentrations in 1889 and  
457 2012 found at Summit were associated with widespread melt events in Greenland, no high  $\underline{r}BC$  concentration peaks were  
458 found in 1889 or 2012 at the SIGMA-D site. As shown in Fig. ~~13~~14 and Table A1, some of the large biomass burning events



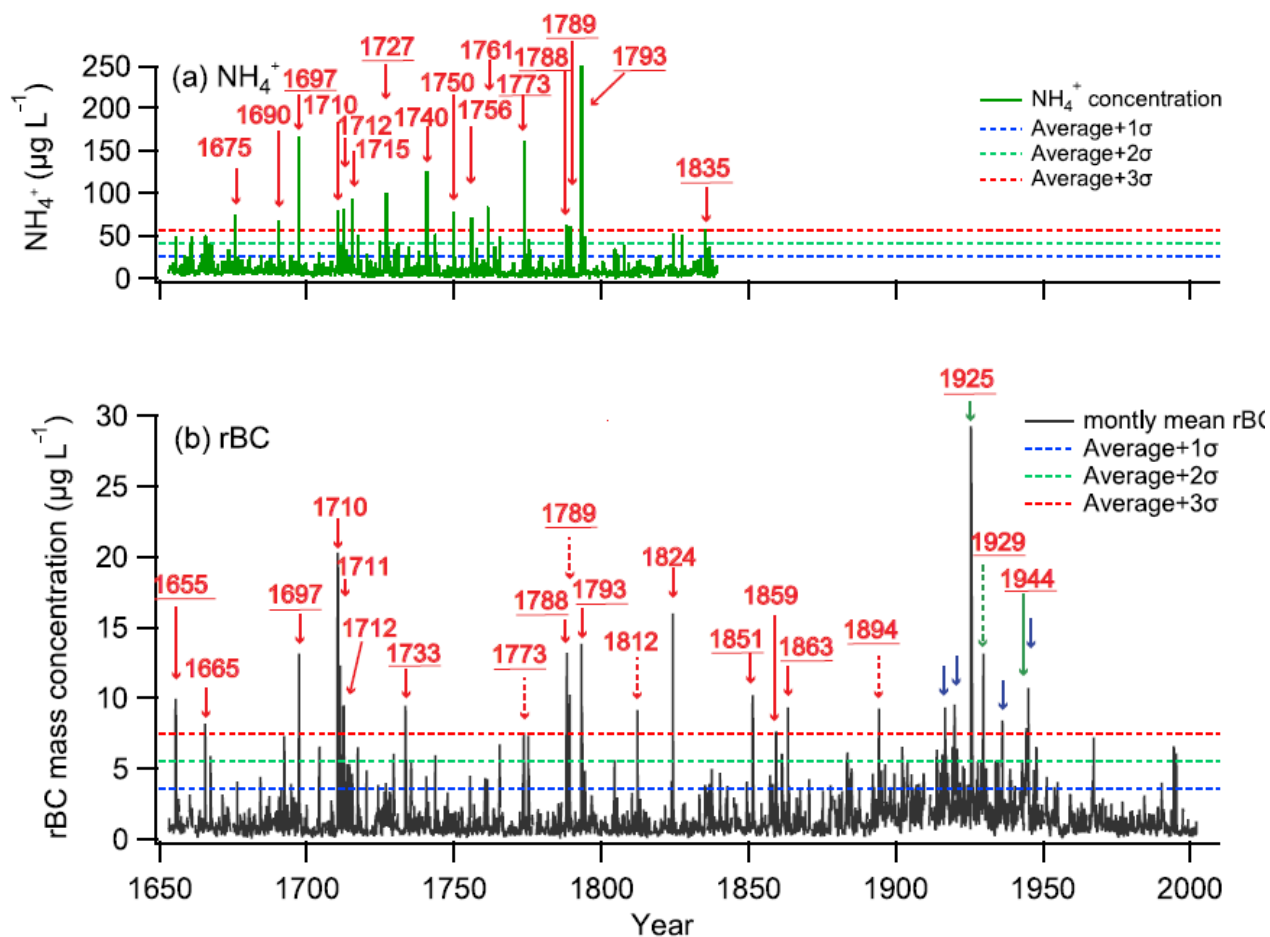


**Figure 1314:** (a)  $\text{NH}_4^+$  concentrations: (a) raw data, and (b) monthly mean rBC mass concentrations (calculated from CFA data). Red arrows in (a) show years when concentrations exceeded the average + 3 $\sigma$  in summer. Solid and broken arrows in (b) show years when concentrations exceeded the summer (May–July) average + 3 $\sigma$  in summer (May–July), and in spring or autumn months (April, August, and September), respectively. Blue arrows in (b) show years when concentrations exceeded the summer average + 3 $\sigma$  in winter. Solid and broken green arrows in (b) show years when concentrations exceeded the summer (May–July) average + 3 $\sigma$  in summer (May–July), and in spring or autumn months (April, August, and September), respectively, but those that might have been affected by winter peaks. Underlining denotes years when biomass burning events were also recorded in other Greenland ice cores/surface snow samples within 2 years. Dotted lines in (a) denote the concentration average over 350 years + 1 $\sigma$  (blue), + 2 $\sigma$  (green), and +3 $\sigma$  (red). Dotted lines in (b) denote summer (May–July) concentration average over 350 years + 1 $\sigma$  (blue), + 2 $\sigma$  (green), and +3 $\sigma$  (red).

459 recorded in other Greenland ice cores were not recorded in the SIGMA-D core, and vice versa. There are two possible reasons  
 460 for this: (1) different ice core sites are not always on the transport pathways of rBC from boreal forest fires (Legrand et al.,

2016), and (2) wind scour at a site can remove snow containing high concentrations of  $rBC$ . Despite the minor regional differences within Greenland, most of the large  $rBC$  concentration peaks caused by large biomass burning events were recorded widely across Greenland. This indicates that high  $rBC$  concentration peaks could be used to synchronize different ice cores in Greenland as reference horizons for dating, as is usually carried out with volcanic sulphate peaks and their signatures detected by DEP (dielectric profiling) and ECM (electrical conductivity measurement) peaks (Rasmussen et al., 2008; Sinnl et al., 2022).

The numbers of large biomass burning events in each 10 years are plotted in Fig. 14-15 using different definitions of a “large” event. Figure 14-15(a) displays the numbers of months with mass concentrations in summer (May–July) exceeding the summer average +  $1\sigma$ ,  $2\sigma$ , and  $3\sigma$ ; Fig. 14-15(b) displays the number of months with number concentrations in summer exceeding the summer average +  $1\sigma$ ,  $2\sigma$ , and  $3\sigma$ . Because large events in April, August, and September were not counted to avoid the potential for impact of anthropogenic  $rBC$ , there would be minor underestimation of the number of large events.

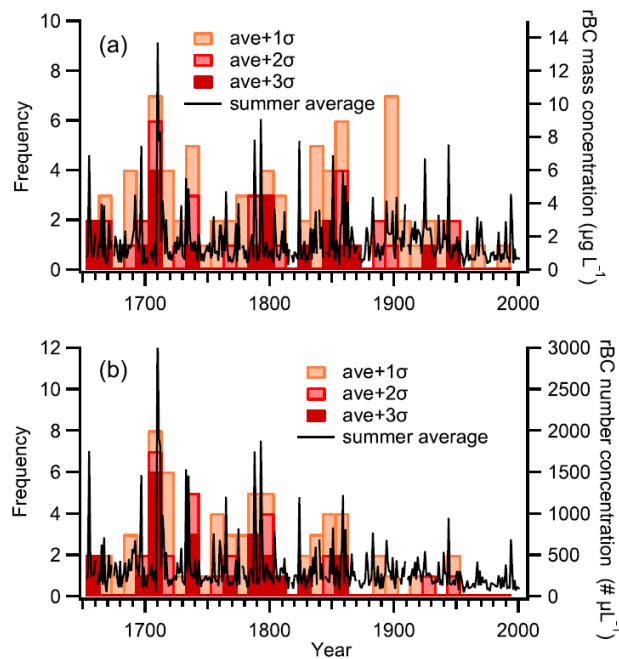


**Figure 14-15: Frequency of large biomass burning events. Black curves denote summer (May–July) averages of  $rBC$  concentrations. Bars show frequency of  $rBC$  summer peaks in each decade exceeding the average +  $1\sigma$ ,  $2\sigma$ , and  $3\sigma$ . (a) Mass concentrations of  $rBC$  were used to define peaks. (b) Number concentrations of  $rBC$  were used to define peaks.**

Although the frequency of large events differs slightly between the different definitions, the general tendency is consistent. Large events tended to be more frequent around the 1710s, 1790s, 1850s, 1900s, and 1950s. Moreover, there is no obvious

473 trend of increase up to the decade 1993–2002. To study the historical trends in concentrations of  $rBC$  originated from biomass  
 474 burning, we calculated the decadal averages of  $rBC$  mass and number concentrations for each month (Fig. 4516). During the  
 475 pre-industrial period, both mass and number concentrations were stable in the winter months (December–February), whereas  
 476 they showed large inter-decadal fluctuations in spring to autumn months (March–November). The fluctuations appear largest

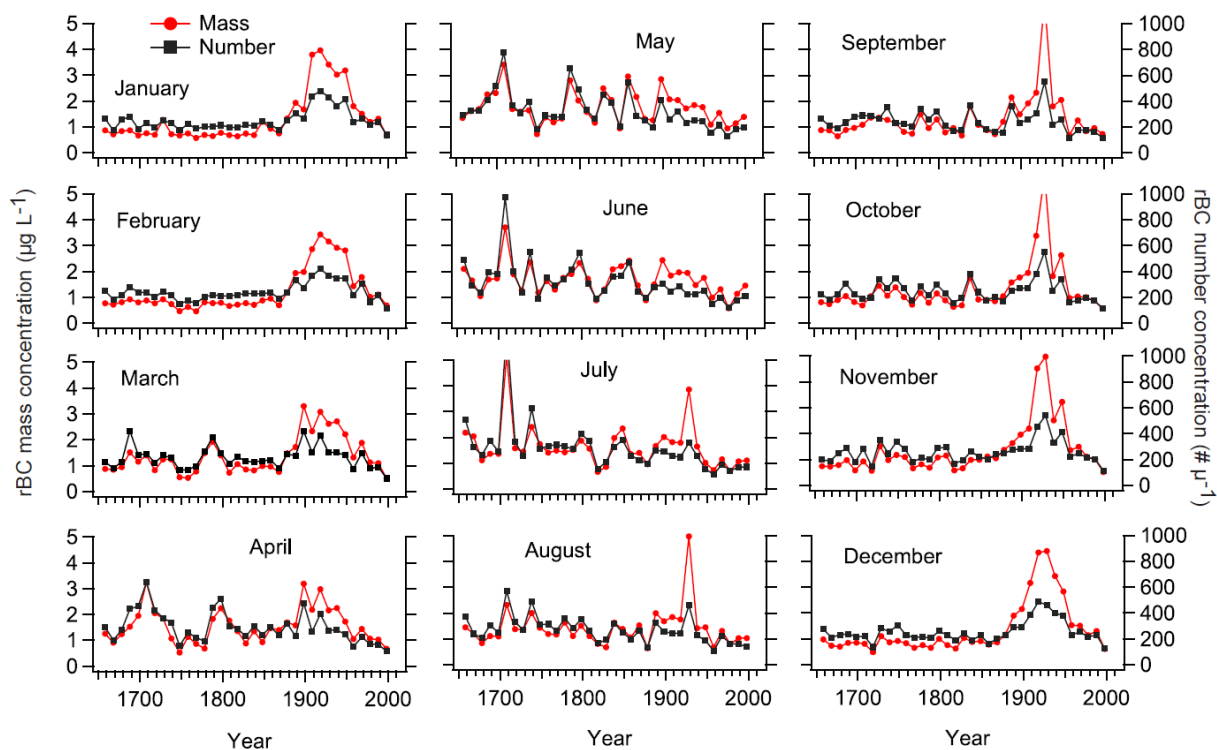


**Figure 4516: Decadal averages of  $rBC$  mass (red) and number (black) concentrations for each month.**

477 in spring–summer (April–July). Generally, the period of April–July is likely when the occurrence of large boreal forest fires  
 478 increases in NA (Whitman et al., 2018). The sporadic nature of the frequency of occurrence of large boreal forest fires would  
 479 explain the large fluctuations.

480 Since the 1870s, when anthropogenic  $rBC$  started to influence the SIGMA-D site,  $rBC$  mass and number  
 481 concentrations in September–April increased, as discussed in Sect. 3.32; however, there was little increase during the spring–  
 482 summer months. The same feature is also seen in Fig. 12(c). Although large inter-decadal variability in concentrations during  
 483 spring–summer obscured the temporal trends in spring–summer concentrations (Fig. 11), the general temporal trends are more  
 484 apparent in Fig. 4516. At the SIGMA-D site, we see slight trends of reduction in  $rBC$  mass and number concentrations during  
 485 spring–summer. Analysis of Fig. 44-15 also suggests that the frequency of large boreal forest fires in NA showed a slight trend

486 of reduction over the past 350 years until the most recent decade (1993–2002). However, this trend has not been reported by  
487 previous studies on other ice cores from Greenland, partly owing to the different periods covered, the different temporal  
488 resolution of the analysis methods, and the different fire proxies used (Zennaro et al., 2014; Legrand et al., 2016; Parvin et al.,  
489 2019; Savarino and Legrand, 1998; Whitlow et al., 1994). Most previous studies used  $\text{NH}_4^+$  as a fire proxy, with occasional  
490 use of levoglucosan and other organic materials; only a few studies have used  $\text{rBC}$  as a fire proxy for pre-industrial periods  
491 (Zennaro et al., 2014).

492 Since the 1950s, data on the area burned and the number of forest fires in Canada have become available (Hanes et  
493 al., 2018; Skakun et al., 2021). The SIGMA-D record does not appear to trace the Canadian forest fire database. Air masses  
494 arriving at the SIGMA-D site might not have passed over Canada during periods of large forest fires. Large uncertainties in  
495 fire data might also explain the disagreement. There are also large uncertainties and regional variability in sedimentary charcoal  
496 fire records (Marlon et al., 2012, 2013; Power et al., 2013). However, our results are consistent with the charcoal data from  
497 western NA, which show general decline in biomass burning since 1500, with a relatively enhanced fire period in the mid-19<sup>th</sup>  
498 century (Power et al., 2013). The biomass burning emission inventories for CMIP 6 also have large uncertainties (van Marle  
499 et al., 2017). Therefore, much more work is needed on the reconstruction of past biomass burning using ice cores.

500

### 501 **3.4 Impacts of $\text{rBC}$ on the ice sheet albedo**

502 McConnell et al. (2007) calculated the quantitative impacts of  $\text{rBC}$  in snow on radiative forcing during early summer using  
503  $\text{rBC}$  concentration from D4 ice core and the Snow, Ice, and Aerosol Radiative (SNICAR) model (Flanner et al., 2007),  
504 assuming an effective snow grain radius of 100  $\mu\text{m}$ . They estimated the radiative forcing of  $1.02 \text{ Wm}^{-2}$  during the peak 5-year  
505 period from 1906 to 1910, ~~representing a fivefold increase compared to which is a fivefold increase from~~ preindustrial  
506 conditions. However, the radiative forcing of  $\text{rBC}$  in snow varies depending on both the assumed solar irradiance and snow  
507 grain size. ~~Then, In this study,~~ we calculated the possible albedo reduction due to  $\text{rBC}$  at the SIGMA-D site from the monthly  
508 mean  $\text{rBC}$  mass concentration data obtained in this study (Fig. 4617) using a physically based snow albedo model (Aoki et al.,  
509 2011). As the snow albedo reduction rate due to light absorbing particles is enhanced with an increase of snow grain size  
510 (Wiscombe and Warren, 1980), we assumed two effective snow grain radii  $r_s = 50 \mu\text{m}$  and  $1000 \mu\text{m}$ , corresponding to new  
511 snow (defined as “precipitation particles” according to Fierz et al., 2009) and old melting snow (defined as “melt forms”  
512 according to Fierz et al., 2009) (Wiscombe and Warren, 1980) for clear sky and cloudy sky (overcast) conditions. The albedo

513 reductions under the cloudy sky are 20-48% larger than those under clear sky. These increases are related to the following two  
 514 factors: (1) the visible albedo depends on  $r_{BC}$  concentration more strongly than the near infrared albedo (Wiscombe and  
 515 Warren, 1980); (2) the visible spectral fraction in solar irradiance at the snow surface under cloudy sky is larger than that under  
 516 clear sky (Aoki et al., 1999). Thus, the albedo reduction due to  $r_{BC}$  under cloudy sky is enhanced more than clear sky.

517 Figure 46-17 demonstrates that the albedo reduction in case of new snow is consistently less than 0.01, even at the  
 518 maximum value for cloudy conditions in August 1925 (Fig. 46a17a). In contrast, for old melting snow, the albedo reduction  
 519 frequently exceeds 0.01 for both sky conditions (Fig. 46b17b). The maximum albedo reduction for cloudy conditions is 0.045  
 520 ( $r_s = 1000 \mu\text{m}$ ) and 0.0098 ( $r_s = 50 \mu\text{m}$ ) in August 1925, followed by the values of 0.034 ( $r_s = 1000 \mu\text{m}$ ) and 0.0074 ( $r_s = 50$   
 521  $\mu\text{m}$ ) in July 1710. The averaged albedo reduction for the overall period of 1650-2014 is 0.0031 ( $r_s = 1000 \mu\text{m}$ ) and 0.0007 ( $r_s$

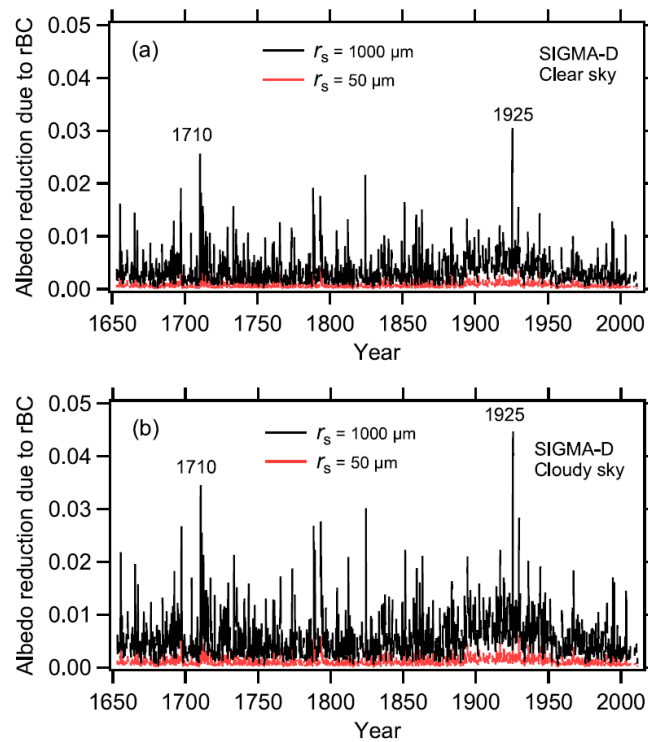


**Figure 46-17:** Temporal variation of albedo reduction for (a) clear sky and (b) cloudy sky conditions, calculated from monthly mean  $r_{BC}$  mass concentrations, for two effective snow grain radii:  $r_s = 50 \mu\text{m}$  (representing new snow, indicated by the red line) and  $r_s = 1000 \mu\text{m}$  (indicating old melting snow, shown by the black line). The albedo reduction values are calculated for solar zenith angle at local solar noon on the 15th of each month, excluding the polar night period from November to February. The maximum albedo reduction is simulated in 1925 and followed by 1710.

522 = 50  $\mu\text{m}$ ) for clear conditions, and 0.0054 ( $r_s = 1000 \mu\text{m}$ ) and 0.0011 ( $r_s = 50 \mu\text{m}$ ) for cloudy conditions. During the  
523 anthropogenic concentration peak period of 1913-1933, the average albedo reduction increases to 0.0056 ( $r_s = 1000 \mu\text{m}$ ) and  
524 0.0012 ( $r_s = 50 \mu\text{m}$ ) for clear conditions, and 0.0089 ( $r_s = 1000 \mu\text{m}$ ) and 0.0019 ( $r_s = 50 \mu\text{m}$ ) for cloudy conditions.

525 Warren ~~et al.~~ (2019) described that an  $\text{rBC}$  concentration of 20 parts per billion in weight can cause broadband snow  
526 albedo reductions of 1-2%. They also noted that for a typical daily average solar irradiance of  $400 \text{ W m}^{-2}$  in the Arctic during  
527 late spring and early summer, a 1% albedo reduction can lead to a positive forcing of  $4 \text{ W m}^{-2}$  locally, similar to the forcing  
528 caused by doubling  $\text{CO}_2$ . Our calculation results indicate that a 1% of reduction in albedo can occur at numerous local spike-  
529 like peaks for  $r_s = 1000 \mu\text{m}$  including the recent several decades after 1950. During the anthropogenic concentration peak  
530 period (1913-1933), the average albedo reduction approaches 1% (0.0089) for  $r_s = 1000 \mu\text{m}$  under cloudy sky conditions.  
531 Consequently, our simulations suggest that the amount of albedo reduction remains relatively small as long as new snow  
532 conditions are maintained. However, if the surface snow grains ~~are reach~~ the size of old melting snow, which would have  
533 occurred during summer months at the SIGMA-D site, the extent of albedo reduction becomes non-negligible.

534

#### 535 4 Conclusions

536 We analysed the record of  $\text{rBC}$  over the past 350 years in the SIGMA-D ice core, which was drilled in northwest Greenland.  
537 The improved technique for  $\text{rBC}$  measurement (Mori et al., 2016) and the CFA system built at NIPR allowed us to reconstruct  
538 high temporal resolution records of the sizes and concentrations of  $\text{rBC}$  particles. Notably, this study marks the first  
539 reconstruction of temporal changes in  $\text{rBC}$  size since the pre-industrial period.

540 The number and mass concentrations of  $\text{rBC}$  started to increase in the 1870s owing to anthropogenic input. The  
541 concentrations reached their maxima in the 1910s–1920s, following which they decreased. By the 1960s,  $\text{rBC}$  concentrations  
542 had reduced to levels close to or lower than those of the pre-industrial period. The trend of anthropogenic  $\text{rBC}$  at the SIGMA-  
543 D site was generally similar to that reported previously for other ice core sites in Greenland, albeit with slight differences.  
544 Backward trajectory analyses suggest that the major anthropogenic emission source that affected the SIGMA-D site was NA.  
545 However, the backward trajectory analyses did not clearly explain the slight difference in the temporal trends of  $\text{rBC}$  between  
546 the SIGMA-D site and the more southerly site D4. Anthropogenic  $\text{rBC}$  was transported to the SIGMA-D site mainly in the  
547 winter half of the year, which was deduced by the changes in the seasonality of  $\text{rBC}$  concentrations. The backward trajectory

548 analyses produced consistent results, showing greater contributions from air masses from the industrial regions in NA, ~~and~~  
549 EUR, ~~and~~ RUS in winter.

550 Pre-industrial  $rBC$  concentrations peaked in summer. In association with increased anthropogenic input,  
551 concentrations increased in winter to early spring, which shifted the annual peak in concentration to winter–early spring. When  
552 the anthropogenic input started to decline in the 1930s, concentrations in winter–early spring also decreased, which changed  
553 the seasonality of  $rBC$  concentrations; by the 1990s,  $rBC$  concentrations peaked in summer once again. This suggests that the  
554 major sources of  $rBC$  in recent years were not anthropogenic emissions but biomass burning. At the SIGMA-D site,  $rBC$   
555 originated from anthropogenic emissions made only a minor contribution to the  $rBC$  concentrations in the summer months  
556 throughout the past 350 years. This enabled us to examine the temporal variability in biomass burning throughout the past 350  
557 years, especially after the increase in anthropogenically derived  $rBC$ , which is a topic that has not been addressed by previous  
558 studies on  $rBC$  data from other ice cores in the Arctic.

559 The size distributions of  $rBC$  particles have also changed owing to anthropogenic impact. The seasonality of MMD  
560 and mBC also changed, accompanying ~~associated with the concentration changes.~~ Both MMD and Winter and summer mBC  
561 started to increase ~~around in~~ the 18230s ~~or~~ 18430s, peaked in the 1910s ~~1890s–1940s–1930s~~ when  $rBC$  concentrations ~~were at~~  
562 ~~their maximum~~ peaked, and started to decline ~~after~~ since the 1940s ~~1930s~~. The winter and summer MMD started to increase in the  
563 1840s and 1810s, respectively, with larger rate of increase for winter MMD. While winter MMD started to decrease in the  
564 1900s – 1920s and has continued to decrease, the summer MMD did not exhibit a clear downward trend. Increases in winter  
565 MMD and mBC ~~accompanying~~ associated with the increase in winter  $rBC$  concentrations suggest that the diameter of  $rBC$   
566 particles deposited over northwest Greenland were generally larger for anthropogenic  $rBC$  than for biomass burning  $rBC$ . ~~The~~  
567 ~~seasonality of MMD and mBC also changed, accompanying the concentration changes.~~ ~~However,~~ ~~i~~n contrast to  $rBC$   
568 concentrations, neither MMD nor mBC returned to their pre-industrial values; instead, they remained at higher values in the  
569 1960s–2000s.

570 Pre-industrial  $rBC$  would have originated mainly from biomass burning. During the winters (December–February) of  
571 the pre-industrial period, decadal averages of monthly mean mass and number concentrations were stable, and the sizes of  $rBC$   
572 particles were smaller than those in summer. This indicates that  $rBC$  in pre-industrial winters originated from biomass burning  
573 in low latitudes where there was no snow cover in winter, and that biomass burning in low latitudes that affected Greenland  
574 showed little change during the pre-industrial period. After the inflow of anthropogenic  $rBC$  started, it became difficult to

575 distinguish biomass burning  $r_{BC}$  from anthropogenic  $r_{BC}$  in winter, making it difficult to discuss the temporal changes in  $r_{BC}$   
576 originated from low-latitude biomass burning in winter. However, we could discuss the temporal changes in boreal forest fires  
577 that occur mainly in summer, the season with minimal anthropogenic input.

578 Sources of pre-industrial  $r_{BC}$  were likely boreal forest fires primarily in NA. We investigated the temporal trend in  
579 the decadal frequency of large boreal forest fire events using high summer peaks of number and mass concentrations of  $r_{BC}$ .  
580 We found no obvious trend of increase in the decadal frequency of large boreal forest fires until the decade of 1993–2002.  
581 Furthermore, we found no trends of increase in the decadal averages of monthly mean mass and number concentrations in  
582 summer during the past 350 years; we even found a trend of decrease for number concentrations. Although recent large fire  
583 events in NA are attributed to global warming (Brown et al., 2023), the effects of global warming do not seem to have left  
584 clear imprint in Greenland until the early 2000s. Therefore, we need further investigations using more recent ice core records  
585 of  $r_{BC}$ .

586 We analysed the temporal variation of potential albedo reduction due to  $r_{BC}$  at the SIGMA-D site during the past  
587 350 years using a physically based snow albedo model. Albedo reductions under the assumption of ~~consistently~~ new snow  
588 grain size remained below 0.01, even at the peak  $r_{BC}$  concentration in 1925. Conversely, under the assumption of old melting  
589 snow grain size, the albedo reduction frequently exceeded 0.01. Our calculation results reveal that a 1% of reduction in albedo  
590 can occur at numerous local spike-like peaks in the case of old melting snow, including the recent several decades after 1950.  
591 During the peak period of anthropogenic concentrations (1913-1933), the averaged albedo reduction approaches 1% for old  
592 melting snow cases. Consequently, our simulations suggest that the magnitude of albedo reduction remains relatively small as  
593 long as new snow conditions are maintained. However, if the surface snow grains ~~are reach~~ the size of old melting snow, the  
594 amount of albedo reduction becomes non-negligible.

595 Our new high temporal resolution records of  $r_{BC}$  concentrations and sizes could contribute to evaluation of the  
596 impacts of both anthropogenically derived and biomass burning originated  $r_{BC}$  on Earth's radiation budget, albedo,  $r_{BC}$ -  
597 cloud interactions, and therefore  $r_{BC}$ -climate interactions. They could also contribute to validation of emission inventories,  
598 and aerosol and climate models. High temporal resolution  $r_{BC}$  data since 2002 are necessary to investigate the impact of global  
599 warming on boreal forest fires. Furthermore, high temporal resolution records of  $r_{BC}$  concentrations and sizes during the early  
600 Holocene and the last interglacial period when it was warmer than the present day (NEEM community members, 2013; Vinther  
601 et al., 2009) should be obtained for better projections of  $r_{BC}$ -climate interactions in a future warming world.





**Figure A1: Monthly snow height change observed with an automatic weather station (AWS) at the SIGMA-D site during the period May 2014 – September 2015 (Matoba et al., 2015). It appears that there was more precipitation in summer than in winter, which could introduce some bias in monthly dating of the SIGMA-D ice core. Although the AWS data indicated that precipitation occurred in all months (Fig. A2), there were a few months when snow height change was negative mainly owing to wind scouring. Moreover, the seasonal variation in precipitation seems to exhibit significant year-to-year variability. However, by averaging monthly mean concentrations over 10-20 years (Fig. 11), we can observe changes in the seasonality of rBC.**

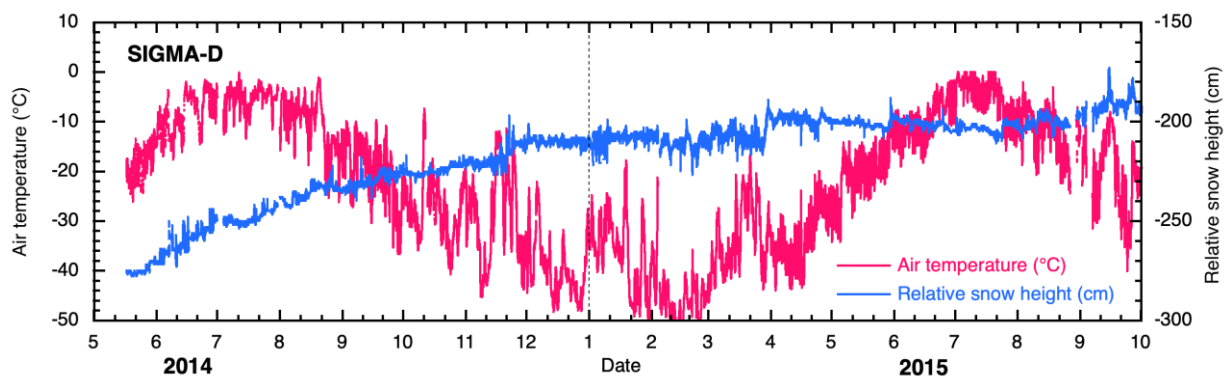


**Figure A2. Seasonal variations of air temperature and relative snow height every 10 minutes observed at the SIGMA-D site during the period May 2014 – September 2015 (Matoba et al., 2015).**

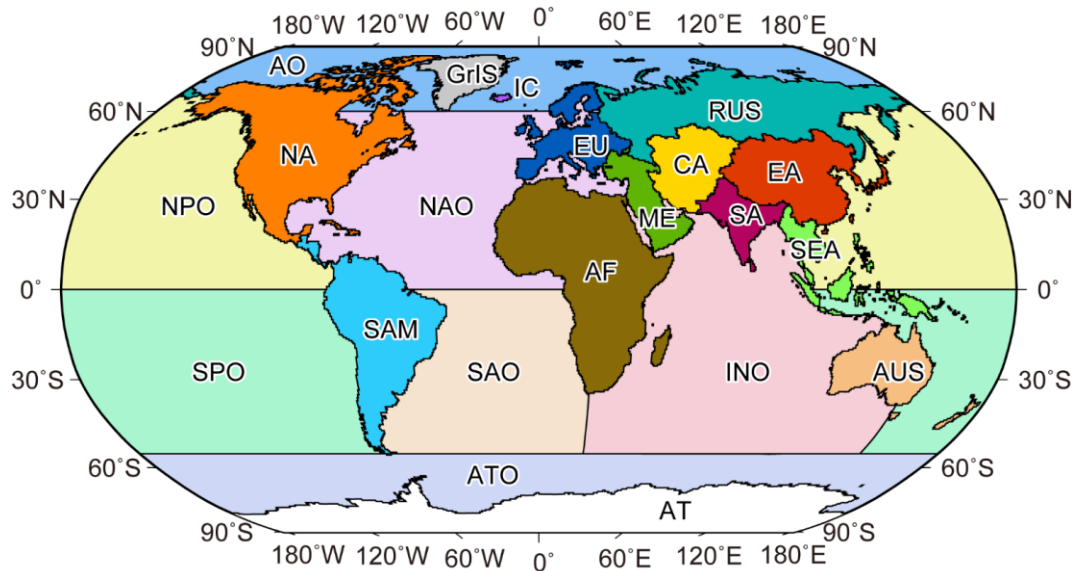


**Figure A3: Map showing 21 regions used for calculating the regional contributions in backward trajectory analysis.**

**ME: Middle East, AT: Antarctica, AUS: Australia and New Zealand, SAM: South America, AF: Africa, EA: China and East Asia, EU: Europe, GrIS: Greenland Ice Sheet, SEA: Southeast Asia, SA: South Asia, CA: Central Asia, RUS: Russia, NA: North America, ATO: Antarctic Ocean, SPO: South Pacific Ocean, INO: Indian Ocean, NPO: North Pacific Ocean, SAO: South Atlantic Ocean, NAO: North Atlantic Ocean, AO: Arctic Ocean, IC: Iceland.**

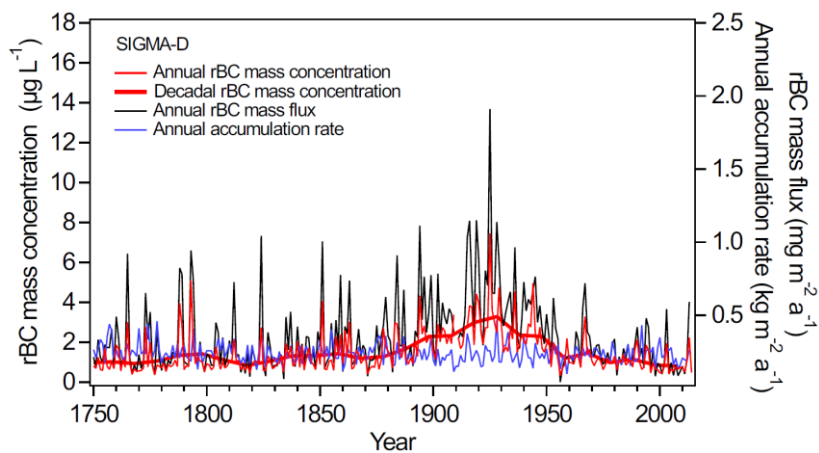


**Figure A4: Annual mean and decadal mean rBC mass concentrations (thin and thick red curves, respectively), annual rBC mass flux (black), and annual accumulation rate (blue).**

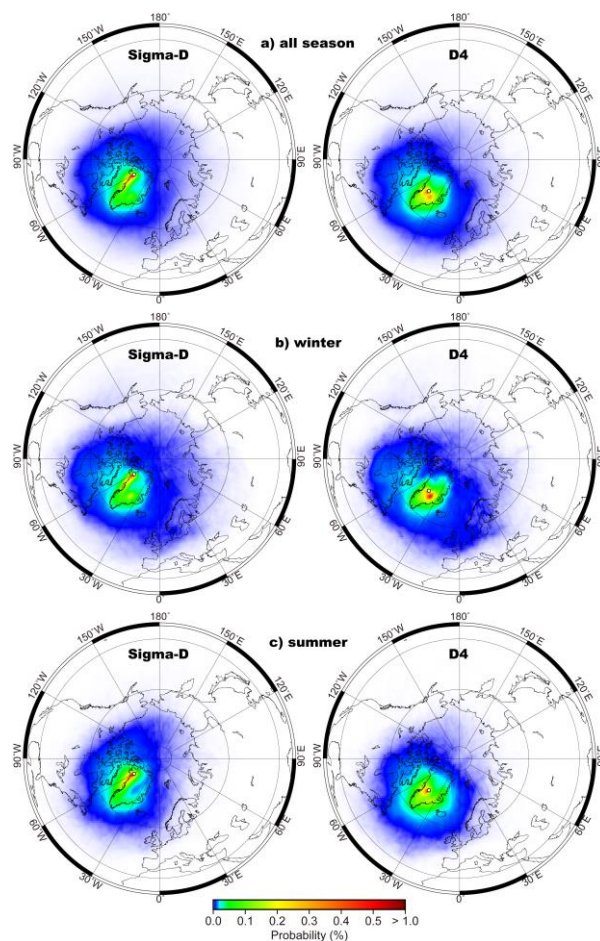


**Figure A5: Probability distributions of air masses at (left) the SIGMA-D site and (right) the D4 site calculated without weighed with the local daily precipitation: (a) averages of all seasons, (b) averages of winter months (December-February), and (c) averages of summer months (May-July).**

608

609 **Table A1 Biomass burning events distinguished in the SIGMA-D ice core record, and in the records of other ice cores**  
610 **and surface snow from Greenland. Records from Greenland sites with temporal resolution of greater than 1 year were**  
611 **not used. Events distinguished in the SIGMA-D core were defined using  $\underline{r}$ BC mass concentration peaks and  $\text{NH}_4^+$**   
612 **concentration peaks. For  $\underline{r}$ BC, peaks exceeding the summer (May–July) averages +  $2\sigma$  or  $3\sigma$  were selected; for  $\text{NH}_4^+$ ,**  
613 **peaks exceeding the annual average +  $2\sigma$  or  $3\sigma$  were selected. If a BC peak was found in April, August, or September,**  
614 **the year is written in parentheses. If an  $\underline{r}$ BC or  $\text{NH}_4^+$  summer peak in the SIGMA-D core with a concentration between**  
615 **the average +  $1\sigma$  and  $2\sigma$  was found in the same year when a large biomass burning event was recorded at other**  
616 **Greenland sites, the peak was also selected as a biomass burning event. If a year with a biomass burning event reported**  
617 **in previous studies agreed with that in the SIGMA-D core within 2 years, the records were considered to reflect the**  
618 **same event, and are written on the same line in the table.**

619 **A: Year of the event in the SIGMA-D core**

620 **B: Magnitude of the  $\underline{r}$ BC mass concentration peak**

621 **C: Magnitude of the  $\text{NH}_4^+$  concentration peak**

622 **D: Year of the event in ice cores and surface snow from Greenland sites other than the SIGMA-D site**

623 **E: Location of the ice core or surface snow in Greenland**

624 **F: Biomass burning proxies**

625 **G: References**

626

SIGMA-D core (This study)			Ice cores and surface snow from Greenland sites other than the SIGMA-D site			
A	B	C	D	E	F	G
Year	Magnitude of $\underline{r}$ BC peak	Magnitude of $\text{NH}_4^+$ peak	Year	Location of ice core or surface snow	Proxy	Reference
1655	>average + $3\sigma$	>average + $2\sigma$	1654 1655	SUMMIT, NEEM SUMMIT	$\text{NH}_4^+$ $\text{NH}_4^+$ , $\text{HCOO}^-$	(Legrand et al., 2016) (Savarino and Legrand, 1998)

1661	No data	>average + 2σ				
1665	>average + 3σ	>average + 2σ				
1667	>average + 2σ	>average + 1σ				
1675		>average + 3σ				
1684	>average + 1σ		1683	NEEM	NH <sub>4</sub> <sup>+</sup>	(Legrand et al., 2016)
1690		>average + 3σ				
1692	>average + 2σ					
1697	>average + 3σ	>average + 3σ	1699	SUMMIT	NH <sub>4</sub> <sup>+</sup>	(Legrand et al., 2016)
			1702–03	NEEM	NH <sub>4</sub> <sup>+</sup>	(Legrand et al., 2016)
			1702	NEEM	<u>r</u> BC	(Zennaro et al., 2014)
			1703	NEEM	<u>r</u> BC	(Zennaro et al., 2014)
1710	>average + 3σ	>average + 3σ				
1711	>average + 3σ	>average + 1σ				
1712	>average + 3σ	>average + 3σ				
1715	>average + 1σ	>average + 3σ				
1717	>average + 1σ	>average + 2σ	1719	NEEM	NH <sub>4</sub> <sup>+</sup>	(Legrand et al., 2016)
1724		>average + 2σ				
1727		>average + 3σ	1728	SUMMIT	NH <sub>4</sub> <sup>+</sup>	(Legrand et al., 2016)
1729	>average + 2σ					
1733	>average + 3σ		1732	NEEM	NH <sub>4</sub> <sup>+</sup>	(Legrand et al., 2016)
1735	>average + 2σ					
1740		>average + 3σ				
1743	>average + 1σ	>average + 2σ				
1750		>average + 3σ				
1756		>average + 3σ				
1761	>average + 1σ	>average + 3σ				

1765	>average + 2σ	>average + 2σ				
1773	>average + 1σ (>average + 3σ in September)	>average + 3σ	1771 1773 1773	NEEM SUMMIT SUMMIT	NH <sub>4</sub> <sup>+</sup> NH <sub>4</sub> <sup>+</sup> NH <sub>4</sub> <sup>+</sup> , HCOO <sup>-</sup>	(Legrand et al., 2016) (Legrand et al., 2016) (Savarino and Legrand, 1998)
1775	>average + 1σ	>average + 2σ				
1788	>average + 3σ	>average + 3σ				
1789	>average + 2σ (>average + 3σ in <del>August</del> April)	>average + 3σ	1789	NEEM	rBC	(Zennaro et al., 2014)
1793	>average + 3σ	>average + 3σ	1792	NEEM	NH <sub>4</sub> <sup>+</sup>	(Legrand et al., 2016)
1794	>average + 1σ	>average + 2σ	1794–95 1795 1795	SUMMIT SUMMIT D4	NH <sub>4</sub> <sup>+</sup> NH <sub>4</sub> <sup>+</sup> , HCOO <sup>-</sup> NH <sub>4</sub> <sup>+</sup>	(Legrand et al., 2016) (Legrand and De Angelis, 1996) (Legrand et al., 2016)
1804	>average + 2σ	>average + 1σ				
1807		>average + 1σ	1807	SUMMIT, NEEM, D4	NH <sub>4</sub> <sup>+</sup>	(Legrand et al., 2016) (Legrand et al., 2016)
(1812)	(>average + 3σ in April)					
1824	>average + 3σ	>average + 2σ				
1827		>average + 2σ				
1835	>average + 1σ	>average + 3σ	1837	SUMMIT, NEEM, D4	NH <sub>4</sub> <sup>+</sup> NH <sub>4</sub> <sup>+</sup>	(Legrand et al., 2016) (Legrand et al., 2016)
1840	>average + 1σ	No data	1839	SUMMIT SUMMIT	NH <sub>4</sub> <sup>+</sup> NH <sub>4</sub> <sup>+</sup> , HCOO <sup>-</sup>	(Legrand et al., 2016) (Legrand and De Angelis, 1996)

			1846	SUMMIT	NH <sub>4</sub> <sup>+</sup>	(Legrand et al., 2016)
1849	>average + 1σ	No data	1847	D4	NH <sub>4</sub> <sup>+</sup>	(Legrand et al., 2016)
			1848	NEEM	NH <sub>4</sub> <sup>+</sup>	(Legrand et al., 2016)
1851	>average + 3σ	No data	1853	NEEM	NH <sub>4</sub> <sup>+</sup>	(Legrand et al., 2016)
		No data	1854	SUMMIT, D4	NH <sub>4</sub> <sup>+</sup>	(Legrand et al., 2016)
1859	>average + 3σ					
1861	>average + 2σ	>average + 1σ				
1863	>average + 3σ	No data	1863	SUMMIT, NEEM, D4 SUMMIT	NH <sub>4</sub> <sup>+</sup> NH <sub>4</sub> <sup>+</sup> NH <sub>4</sub> <sup>+</sup> , HCOO <sup>-</sup>	(Legrand et al., 2016) (Legrand et al., 2016) (Savarino and Legrand, 1998)
		No data	1868	SUMMIT	NH <sub>4</sub> <sup>+</sup>	(Keegan et al., 2014)
			1869	D4	NH <sub>4</sub> <sup>+</sup>	(Legrand et al., 2016)
	No data	No data	1871	SUMMIT	NH <sub>4</sub> <sup>+</sup>	(Legrand et al., 2016)
			1872, D4	NEEM	NH <sub>4</sub> <sup>+</sup>	(Legrand et al., 2016)
1883	>average + 2σ	No data				
		No data	1886	SUMMIT, NEEM, D4 20D (Dye-3), GISP2 (SUMMIT)	NH <sub>4</sub> <sup>+</sup> NH <sub>4</sub> <sup>+</sup> NH <sub>4</sub> <sup>+</sup>	(Legrand et al., 2016) (Legrand et al., 2016) (Whitlow et al., 1994) (Legrand et al., 2016)
			1888	NEEM	NH <sub>4</sub> <sup>+</sup>	
		No data	1889	SUMMIT	<u>1</u> BC, NH <sub>4</sub> <sup>+</sup>	(Keegan et al., 2014)
				D4	NH <sub>4</sub> <sup>+</sup>	(Legrand et al., 2016)
			1890	SUMMIT	NH <sub>4</sub> <sup>+</sup>	(Legrand et al., 2016)

1894	>average + 1σ (>average + 3σ in April)	No data	1894–95 1894–95 1895	SUMMIT, NEEM, D4 SUMMIT	NH <sub>4</sub> <sup>+</sup> NH <sub>4</sub> <sup>+</sup> NH <sub>4</sub> <sup>+</sup> , HCOO <sup>-</sup>	(Legrand et al., 2016) (Legrand et al., 2016) (Legrand and De Angelis, 1996)
1896	>average + 1σ	No data	1896	SUMMIT	NH <sub>4</sub> <sup>+</sup> , HCOO <sup>-</sup>	(Savarino and Legrand, 1998)
1902	>average + 2σ	No data				
1909	>average + 1σ	No data	1908	SUMMIT, D4 SUMMIT SUMMIT	NH <sub>4</sub> <sup>+</sup> NH <sub>4</sub> <sup>+</sup> , HCOO <sup>-</sup> rBC, NH <sub>4</sub> <sup>+</sup>	(Legrand et al., 2016) (Savarino and Legrand, 1998) (Keegan et al., 2014)
		No data	1921	NEEM	NH <sub>4</sub> <sup>+</sup>	(Legrand et al., 2016)
1925	>average + 3σ	No data	1923	SUMMIT, D4	NH <sub>4</sub> <sup>+</sup>	(Legrand et al., 2016)
1927	>average + 1σ	No data	1927–28	NEEM	NH <sub>4</sub> <sup>+</sup>	(Legrand et al., 2016)
(1929)	(>average + 3σ in <del>August</del> & September & <del>October</del> )		1929	SUMMIT, D4	NH <sub>4</sub> <sup>+</sup>	(Legrand et al., 2016)
1936	>average + 1σ	No data	1936–38 1938	SUMMIT SUMMIT, NEEM, D4	NH <sub>4</sub> <sup>+</sup> NH <sub>4</sub> <sup>+</sup>	(Legrand et al., 2016) (Legrand et al., 2016)
1940	>average + 1σ	No data				
1944	>average + 3σ	No data	1942	NEEM, D4	NH <sub>4</sub> <sup>+</sup>	(Legrand et al., 2016)
		No data	1950	SUMMIT, NEEM, D4 SUMMIT	NH <sub>4</sub> <sup>+</sup> NH <sub>4</sub> <sup>+</sup> , HCOO <sup>-</sup>	(Legrand et al., 2016) (Savarino and Legrand, 1998)



		No data	1961	SUMMIT, NEEM, D4	NH <sub>4</sub> <sup>+</sup>	(Legrand et al., 2016)
		No data		SUMMIT	NH <sub>4</sub> <sup>+</sup> , HCOO <sup>-</sup>	(Savarino and Legrand, 1998)
		No data		SE-Dome	Levogluconan	(Parvin et al., 2019)
		No data	1964	SE-Dome	Levogluconan	(Parvin et al., 2019)
		No data	1972	NEEM	rBC	(Zennaro et al., 2014)
		No data	1973	NEEM	NH <sub>4</sub> <sup>+</sup>	(Legrand et al., 2016)
		No data	1980	SUMMIT, NEEM, D4	NH <sub>4</sub> <sup>+</sup>	
1994	>average + 2σ	No data	1994	SE-Dome SUMMIT	Levogluconan, Levogluconan, NH <sub>4</sub> <sup>+</sup> , HCOO <sup>-</sup> , CH <sub>3</sub> COO <sup>-</sup> , (C <sub>2</sub> H <sub>2</sub> O <sub>4</sub> ) <sup>2-</sup>	(Parvin et al., 2019) (Kehrwald et al., 2012; Dibb et al., 1996)
1995	>average + 2σ	No data				
		No data	1998	SE-Dome	Levogluconan	(Parvin et al., 2019)
	No CFA data	No data	2012	SUMMIT	rBC, NH <sub>4</sub>	(Keegan et al., 2014)
	No CFA data	No data	2013	SE-Dome	Levogluconan	(Parvin et al., 2019)

627

628

629

### Appendix B: Wet deposition vs dry deposition

630

We anticipate that the contribution of wet deposition was greater than that of dry deposition. It is difficult to estimate

631

the wet and dry deposition ratio directly since there are no observations at the SIGMA-D site, as at most of the sites in

632

the Arctic. Instead, we estimated the terminal velocity (V) of rBC particles falling onto the SIGMA-D site using the

633

equation  $V=2\rho r^2g/9\zeta$  assuming spherical rBC particles. Here  $\rho$ ,  $r$ ,  $g$ , and  $\zeta$  denote the density of rBC particles, the radius

634 of rBC particles, the acceleration of gravity, and the viscosity coefficient of the atmosphere, respectively. We used the  
635 values 1800 kg m<sup>-3</sup> and 1 μm for ρ and 2r (diameter), respectively. Assuming an atmospheric temperature of -40°C, ζ  
636 was calculated to be 1.5×10<sup>-5</sup> N s m<sup>-2</sup>. With these values, the terminal velocity was estimated to be 6 m day<sup>-1</sup>. Given that  
637 the rBC particles fall from 500 m above the ice sheet surface at the SIGMA-D site, it would take approximately 100 days  
638 for the rBC particles to reach the ice sheet surface, indicating a very small dry deposition velocity at the SIGMA-D site.  
639 A study using the GEOS-Chem global chemical transport model (Breider et al., JGR, 2014) also indicated that the annual  
640 mean fraction of dry deposition in the Arctic was only 11 %. Furthermore, Sinha et al. (JGR, 2018) showed that the dry  
641 deposition was a small contributor (less than the uncertainties of the measurements, which were about 20%) to the total  
642 rBC deposition at Ny-Ålesund, Svalbard, where the total water equivalent snowfall amount during September-April was  
643 similar to the annual accumulation rate at the SIGMA-D site. Thus, it is reasonable to assume that the contribution of  
644 dry deposition is small.

#### 645

#### 646 **Data availability**

647 All the data used in this study will be submitted to the Arctic Data Archive System (ADS) as soon as the manuscript has been  
648 published.

#### 649

#### 650 **Author contributions**

651 KGA designed the study and led the manuscript writing. YOT was responsible for the BC measurements. YOT, MH, RD, and  
652 JO performed the CFA analyses of the SIGMA-D core. MH and SM measured the ion concentrations in the discrete samples.  
653 KoF, SM, AT, and NN dated the SIGMA-D ice core. MK calculated annual accumulation rates. KGA, YOT, and KaF analysed  
654 the CFA data. KGA, YOT, NM, TM, SO, YK, and MK interpreted the BC data. KoF performed backward trajectory analyses.  
655 TA analysed the AWS data. SM examined the melt features in the SIGMA-D ice core. TA designed and led the ice coring  
656 project at SIGMA-D. TA computed the impacts of BC on albedo. All the authors discussed the results.

#### 657

#### 658 **Competing interests**

659 The authors declare that they have no conflict of interest.

661 **Acknowledgements**

662 We would like to thank Hideaki Motoyama, Tetsuhide Yamasaki, Masahiro Minowa, Yukihiro Onuma, and Yuki Komuro  
663 ~~who for drilled~~ the SIGMA-D core, ~~and Yuki Komuro who cut and processing ed the core it~~ in the field, and installing the  
664 AWS at the SIGMA-D site. This study has been supported by JSPS KAKENHI (Grant Numbers: JP 22221002, JP23221004,  
665 and JP18H04140), the Arctic Challenge for Sustainability (ArCS) Project (Program Grant Number: JPMXD130000000), the  
666 Arctic Challenge for Sustainability II (ArCS II) Project (Program Grant Number: JPMXD1420318865), and the Environment  
667 Research and Technology Development Funds (JPMEERF20172003, JPMEERF20202003 and JPMEERF20232001) of the  
668 Environmental Restoration and Conservation Agency of Japan. We thank three anonymous reviewers for their valuable and  
669 insightful comments. James Buxton MSc, from Edanz (<https://jp.edanz.com/ac>), for editing a draft of this manuscript.

670

671 **References**

- 672 Aoki, T., Aoki, T., Fukabori, M., and Uchiyama, A.: Numerical Simulation of the Atmospheric Effects on Snow Albedo with  
673 a Multiple Scattering Radiative Transfer Model for the Atmosphere-Snow System, *J. Meteorol. Soc. of Japan. Ser. II*,  
674 77, 595–614, doi:10.2151/jmsj1965.77.2\_595, 1999.
- 675 Aoki, T., Kuchiki, K., Niwano, M., Kodama, Y., Hosaka, M., and Tanaka, T.: Physically based snow albedo model for  
676 calculating broadband albedos and the solar heating profile in snowpack for general circulation models, *J. Geophys.*  
677 *Res. Atmos.*, 116, D11114, doi:10.1029/2010JD015507, 2011.
- 678 Bauer, S. E., Bausch, A., Nazarenko, L., Tsigaridis, K., Xu, B., Edwards, R., Bisiaux, M., and McConnell, J.: Historical and  
679 future black carbon deposition on the three ice caps: Ice core measurements and model simulations from 1850 to 2100, *J.*  
680 *Geophys. Res.-Atmos.*, 118, 7948–7961, doi:10.1002/jgrd.50612, 2013.
- 681 Baumgardner, D., Kok, G., and Raga, G.: Warming of the Arctic lower stratosphere by light absorbing particles, *Geophys.*  
682 *Res. Lett.*, 31, <https://doi.org/10.1029/2003GL018883>, 2004.
- 683 Bisiaux, M. M., Edwards, R., McConnell, J. R., Albert, M. R., Anschütz, H., Neumann, T. A., Isaksson, E., and Penner, J. E.:  
684 Variability of black carbon deposition to the East Antarctic Plateau, 1800–2000 AD, *Atmos. Chem. Phys.*, 12, 3799–3808,  
685 10.5194/acp-12-3799-2012, 2012a.

686 Bisiaux, M. M., Edwards, R., McConnell, J. R., Curran, M. A. J., Van Ommen, T. D., Smith, A. M., Neumann, T. A., Pasteris,  
687 D. R., Penner, J. E., and Taylor, K.: Changes in black carbon deposition to Antarctica from two high-resolution ice core  
688 records, 1850–2000 AD, *Atmos. Chem. Phys.*, 12, 4107–4115, 10.5194/acp-12-4107-2012, 2012b.

689 Bond, T. C., Doherty, S. J., Fahey, D. W., Forster, P. M., Berntsen, T., DeAngelo, B. J., Flanner, M. G., Ghan, S., Kärcher, B.,  
690 Koch, D., Kinne, S., Kondo, Y., Quinn, P. K., Sarofim, M. C., Schultz, M. G., Schulz, M., Venkataraman, C., Zhang, H.,  
691 Zhang, S., Bellouin, N., Guttikunda, S. K., Hopke, P. K., Jacobson, M. Z., Kaiser, J. W., Klimont, Z., Lohmann, U., Schwarz,  
692 J. P., Shindell, D., Storelvmo, T., Warren, S. G., and Zender, C. S.: Bounding the role of black carbon in the climate system:  
693 A scientific assessment, *J. Geophys. Res.-Atmos.* n/a-n/a, 10.1002/jgrd.50171, 2013.

694 Breider, T. J., Mickley, L. J., Jacob, D. J., Ge, C., Wang, J., Payer Sulprizio, M., Croft, B., Ridley, D. A., McConnell, J. R.,  
695 Sharma, S., Husain, L., Dutkiewicz, V. A., Eleftheriadis, K., Skov, H., and Hopke, P. K.: Multidecadal trends in aerosol  
696 radiative forcing over the Arctic: Contribution of changes in anthropogenic aerosol to Arctic warming since 1980, *J.*  
697 *Geophys. Res.-Atmos.*, 10.1002/2016JD025321, 2017.

698 Brown, P. T., Hanley, H., Mahesh, A., Reed, C., Strenfel, S. J., Davis, S. J., Kochanski, A. K., and Clements, C. B.: Climate  
699 warming increases extreme daily wildfire growth risk in California, *Nature*, 621, 760–766, 10.1038/s41586-023-06444-3,  
700 2023.

701 Calkin, D. E., Barrett, K., Cohen, J. D., Finney, M. A., Pyne, S. J., and Quarles, S. L.: Wildland-urban fire disasters aren't  
702 actually a wildfire problem, *P. Natl. Acad. Sci.*, 120, e2315797120, doi:10.1073/pnas.2315797120, 2023.

703 [de la Casa, A. and Nasello, O.: Breakpoints in annual rainfall trends in Córdoba, Argentina, \*Atmos. Res.\*, 95, 419–417,](#)  
704 [2010.](#)

705 Dibb, J. E., Talbot, R. W., Whitlow, S. I., Shipham, M. C., Winterle, J., McConnell, J., and Bales, R.: Biomass burning  
706 signatures in the atmosphere and snow at Summit, Greenland: An event on 5 August 1994, *Atmos. Environ.*, 30, 553–561,  
707 10.1016/1352-2310(95)00328-2, 1996.

708 Du, Z.-H., Xiao, C.-D., Dou, T.-F., Li, C.-J., Ding, M.-H., Sharma, S., Ma, X.-Y., Wang, S.-M., and Zhang, W.-B.: A shallow  
709 ice core from East Greenland showing a reduction in black carbon during 1990–2016, *Adv. Clim. Change Res.*, 11, 360–  
710 369, <https://doi.org/10.1016/j.accre.2020.11.009>, 2020.

711 Eckhardt, S., Pisso, I., Evangeliou, N., Zwaafink, C. G., Plach, A., McConnell, J. R., Sigl, M., Ruppel, M., Zdanowicz, C.,  
712 Lim, S., Chellman, N., Opel, T., Meyer, H., Steffensen, J. P., Schwikowski, M., and Stohl, A.: Revised historical Northern

713 Hemisphere black carbon emissions based on inverse modeling of ice core records, *Nat. Commun.*, 14, 271,  
714 10.1038/s41467-022-35660-0, 2023.

715 Fierz, C., Armstrong, R.L., Durand, Y., Etchevers, P., Greene, E., McClung, D.M., Nishimura, K., Satyawali, P.K. and  
716 Sokratov, S.A.: The International Classification for Seasonal Snow on the Ground, IHP-VII Technical Documents in  
717 Hydrology N°83, IACS Contribution N°1, UNESCO-IHP, Paris, 2009.

718 Fischer, H., Schupbach, S., Gfeller, G., Bigler, M., Rothlisberger, R., Erhardt, T., Stocker, T. F., Mulvaney, R., and Wolff, E.  
719 W.: Millennial changes in North American wildfire and soil activity over the last glacial cycle, *Nature Geosci.*, 8, 723–727,  
720 doi:10.1038/ngeo2495, 2015.

721 Flanner, M. G., Zender, C. S., Randerson, J. T., and Rasch, P. J.: Present-day climate forcing and response from black carbon  
722 in snow, *J. Geophys. Res.* 112, doi:10.1029/2006JD008003, 2007.

723 Gong, S. L., Zhao, T. L., Sharma, S., Toom-Sauntry, D., Lavoué, D., Zhang, X. B., Leaitch, W. R., and Barrie, L. A.:  
724 Identification of trends and interannual variability of sulfate and black carbon in the Canadian High Arctic: 1981–2007, *J.*  
725 *Geophys. Res.-Atmos.*, 115, <https://doi.org/10.1029/2009JD012943>, 2010.

726 Goto-Azuma, K. and Koerner, R. M.: Ice core studies of anthropogenic sulfate and nitrate trends in the Arctic, *J. Geophys.*  
727 *Res.-Atmos.*, 106, 4959–4969, 2001.

728 Goto-Azuma, K., [Dallmayr, R., Ogawa-Tsukagawa, Y., Moteki, N., Mori, T., Ohata, S., Kondo, Y., Koike, M., Hirabayashi,](#)  
729 [M., Ogata, J., Kitamura, K., Kawamura, K., Fujita, K., Matoba, S., Nagatsuka, N., Tsushima, A., Fukuda, K., and Aoki,](#)  
730 [T.](#) ~~Coauthors TBD~~: Technical note: High-resolution analyses of concentrations and sizes of black carbon particles deposited  
731 on northwest Greenland over the past 350 years – Part 1. Continuous flow analysis of the SIGMA-D ice core using a Wide-  
732 Range Single-Particle Soot Photometer and a high-efficiency nebulizer, ~~submitted to~~ [accepted by](#) *Atmos. Phys. Chem.*

733 Grieman, M. M., Aydin, M., Fritzsche, D., McConnell, J. R., Opel, T., Sigl, M., and Saltzman, E. S.: Aromatic acids in a  
734 Eurasian Arctic ice core: a 2600-year proxy record of biomass burning, *Clim. Past*, 13, 395–410, 10.5194/cp-13-395-2017,  
735 2017.

736 Grieman, M. M., Aydin, M., McConnell, J. R., and Saltzman, E. S.: Burning-derived vanillic acid in an Arctic ice core from  
737 Tunu, northeastern Greenland, *Clim. Past*, 14, 1625–1637, 10.5194/cp-14-1625-2018, 2018.

738 Hanes, C. C., Wang, X., Jain, P., Parisien, M.-A., Little, J. M., and Flannigan, M. D.: Fire-regime changes in Canada over the  
739 last half century, *Can. J. Forest Res.*, 49, 256–269, 10.1139/cjfr-2018-0293, 2018.

740 Hennigan, C. J., Sullivan, A. P., Collett Jr., J. L., and Robinson, A. L.: Levoglucosan stability in biomass burning particles  
741 exposed to hydroxyl radicals, *Geophys. Res. Lett.*, 37, <https://doi.org/10.1029/2010GL043088>, 2010.

742 Hersbach, H., Bell, B., Berrisford, P., Hirahara, S., Horányi, A., Muñoz-Sabater, J., Nicolas, J., Peubey, C., Radu, R., Schepers,  
743 D., Simmons, A., Soci, C., Abdalla, S., Abellan, X., Balsamo, G., Bechtold, P., Biavati, G., Bidlot, J., Bonavita, M., De  
744 Chiara, G., Dahlgren, P., Dee, D., Diamantakis, M., Dragani, R., Flemming, J., Forbes, R., Fuentes, M., Geer, A.,  
745 Haimberger, L., Healy, S., Hogan, R. J., Hólm, E., Janisková, M., Keeley, S., Laloyaux, P., Lopez, P., Lupu, C., Radnoti,  
746 G., de Rosnay, P., Rozum, I., Vamborg, F., Villaume, S., and Thépaut, J.-N.: The ERA5 global reanalysis, *Q. J. Roy. Meteor.  
747 Soc.*, 146, 1999–2049, <https://doi.org/10.1002/qj.3803>, 2020.

748 Hoesly, R. M., Smith, S. J., Feng, L., Klimont, Z., Janssens-Maenhout, G., Pitkanen, T., Seibert, J. J., Vu, L., Andres, R. J.,  
749 Bolt, R. M., Bond, T. C., Dawidowski, L., Kholod, N., Kurokawa, J. I., Li, M., Liu, L., Lu, Z., Moura, M. C. P., O'Rourke,  
750 P. R., and Zhang, Q.: Historical (1750–2014) anthropogenic emissions of reactive gases and aerosols from the Community  
751 Emissions Data System (CEDS), *Geosci. Model Dev.*, 11, 369–408, [10.5194/gmd-11-369-2018](https://doi.org/10.5194/gmd-11-369-2018), 2018.

752 Jurányi, Z., Zanatta, M., Lund, M. T., Samset, B. H., Skeie, R. B., Sharma, S., Wendisch, M., and Herber, A.: Atmospheric  
753 concentrations of black carbon are substantially higher in spring than summer in the Arctic, *Comm. Earth Environ.*, 4, 91,  
754 [10.1038/s43247-023-00749-x](https://doi.org/10.1038/s43247-023-00749-x), 2023.

755 Kaspari, S. D., Schwikowski, M., Gysel, M., Flanner, M. G., Kang, S., Hou, S., and Mayewski, P. A.: Recent increase in black  
756 carbon concentrations from a Mt. Everest ice core spanning 1860–2000 AD, *Geophys. Res. Lett.*, 38, L04703,  
757 [10.1029/2010gl046096](https://doi.org/10.1029/2010gl046096), 2011.

758 Kawamura, K., Izawa, Y., Mochida, M., and Shiraiwa, T.: Ice core records of biomass burning tracers (levoglucosan and  
759 dehydroabietic, vanillic and p-hydroxybenzoic acids) and total organic carbon for past 300 years in the Kamchatka  
760 Peninsula, Northeast Asia, *Geochim. Cosmochim. Acta*, 99, <https://doi.org/10.1016/j.gca.2012.08.006> 317–329, 2012.

761 Keane, R. E., Agee, J. K., Fulé, P., Keeley, J. E., Key, C., Kitchen, S. G., Miller, R., and Schulte, L. A.: Ecological effects of  
762 large fires on US landscapes: benefit or catastrophe? *Int. J. Wildland Fire*, 17, 696–712, <https://doi.org/10.1071/WF07148>,  
763 2008.

764 Keegan, K. M., Albert, M. R., McConnell, J. R., and Baker, I.: Climate change and forest fires synergistically drive widespread  
765 melt events of the Greenland Ice Sheet, *P. Natl. Acad. Sci.*, 111, 7964–7967, [10.1073/pnas.1405397111](https://doi.org/10.1073/pnas.1405397111), 2014.

766 Keeley, J. E. and Syphard, A. D.: Large California wildfires: 2020 fires in historical context, *Fire Ecology*, 17, 22,  
767 10.1186/s42408-021-00110-7, 2021.

768 Kehrwald, N., Zangrando, R., Gabrielli, P., Jaffrezo, J.-L., Boutron, C., Barbante, C., and Gambaro, A.: Levoglucosan as a  
769 specific marker of fire events in Greenland snow, *Tellus B: Chem. Phys. Meteorol.*, 64, 18196, 10.3402/tellusb.v64i0.18196,  
770 2012.

771 Lamarque, J. F., Bond, T. C., Eyring, V., Granier, C., Heil, A., Klimont, Z., Lee, D., Liousse, C., Mieville, A., Owen, B.,  
772 Schultz, M. G., Shindell, D., Smith, S. J., Stehfest, E., Van Aardenne, J., Cooper, O. R., Kainuma, M., Mahowald, N.,  
773 McConnell, J. R., Naik, V., Riahi, K., and van Vuuren, D. P.: Historical (1850–2000) gridded anthropogenic and biomass  
774 burning emissions of reactive gases and aerosols: methodology and application, *Atmos. Chem. Phys.*, 10, 7017–7039,  
775 10.5194/acp-10-7017-2010, 2010.

776 Legrand, M. and De Angelis, M.: Light carboxylic acids in Greenland ice: A record of past forest fires and vegetation emissions  
777 from the boreal zone, *J. Geophys. Res.-Atmos.*, 101, 4129–4145, <https://doi.org/10.1029/95JD03296>, 1996.

778 Legrand, M. and Mayewski, P.: Glaciochemistry of polar ice cores: A review, *Rev. Geophys.*, 35, 219–243,  
779 10.1029/96RG03527, 1997.

780 Legrand, M., De Angelis, M., Staffelbach, T., Neftel, A., and Stauffer, B.: Large perturbations of ammonium and organic acids  
781 in the Summit-Greenland ice core. Fingerprint from forest fires? *Geophys. Res. Lett.*, 19, 473–475,  
782 <http://dx.doi.org/10.1029/91GL03121>, 1992.

783 Legrand, M., McConnell, J., Fischer, H., Wolff, E. W., Preunkert, S., Arienzo, M., Chellman, N., Leuenberger, D., Maselli,  
784 O., Place, P., Sigl, M., Schüpbach, S., and Flannigan, M.: Boreal fire records in Northern Hemisphere ice cores: A review,  
785 *Clim. Past*, 12, 2033–2059, 10.5194/cp-12-2033-2016, 2016.

786 [Lim, S., Fäin, X., Zanatta, M., Cozic, J., Jaffrezo, J.-L., Ginot, P., and Laj, P.: Refractory black carbon mass concentrations](#)  
787 [in snow and ice: method evaluation and inter-comparison with elemental carbon measurement, \*Atmos. Meas. Tech.\*, 7,](#)  
788 [3307-3324. doi: 10.5194/amt-7-3307-2014, 2014.](#)

789 Marlon, J. R., Bartlein, P. J., Gavin, D. G., Long, C. J., Anderson, R. S., Briles, C. E., Brown, K. J., Colombaroli, D., Hallett,  
790 D. J., Power, M. J., Scharf, E. A., and Walsh, M. K.: Long-term perspective on wildfires in the western USA, *P. Natl. Acad.*  
791 *Sci.*, 109, E535–E543, 10.1073/pnas.1112839109, 2012.

792 Marlon, J. R., Bartlein, P. J., Daniau, A.-L., Harrison, S. P., Maezumi, S. Y., Power, M. J., Tinner, W., and Vanni re, B.:  
793 Global biomass burning: a synthesis and review of Holocene paleofire records and their controls, *Quaternary Sci. Rev.*, 65,  
794 5–25, <http://dx.doi.org/10.1016/j.quascirev.2012.11.029>, 2013.

795 Marlon, J. R., Kelly, R., Daniau, A. L., Vanni re, B., Power, M. J., Bartlein, P., Higuera, P., Blarquez, O., Brewer, S., Br ucher,  
796 T., Feurdean, A., Romera, G. G., Iglesias, V., Maezumi, S. Y., Magi, B., Courtney Mustaphi, C. J., and Zhihai, T.:  
797 Reconstructions of biomass burning from sediment-charcoal records to improve data–model comparisons, *Biogeosciences*,  
798 13, 3225–3244, 10.5194/bg-13-3225-2016, 2016.

799 Massling, A., Nielsen, I. E., Kristensen, D., Christensen, J. H., S rensen, L. L., Jensen, B., Nguyen, Q. T., N jgaard, J. K.,  
800 Glasius, M., and Skov, H.: Atmospheric black carbon and sulfate concentrations in Northeast Greenland, *Atmos. Chem.*  
801 *Phys.*, 15, 9681–9692, 10.5194/acp-15-9681-2015, 2015.

802 Matoba, S., Motoyama, H., Fujita, K., Yamasaki, T., Minowa, M., Onuma, Y., Komuro, Y., Aoki, T., Yamaguchi, S.,  
803 Sugiyama, S., and Enomoto, H.: Glaciological and meteorological observations at the SIGMA-D site, northwestern  
804 Greenland Ice Sheet, *B. Glaciol. Res.*, 33, 7–14, 10.5331/bgr.33.7, 2015.

805 Matsui, H., Mori, T., Ohata, S., Moteki, N., Oshima, N., Goto-Azuma, K., Koike, M., and Kondo, Y.: Contrasting source  
806 contributions of Arctic black carbon to atmospheric concentrations, deposition flux, and atmospheric and snow radiative  
807 effects, *Atmos. Chem. Phys.*, 22, 8989–9009, 10.5194/acp-22-8989-2022, 2022.

808 McConnell, J. R.: New Directions: Historical black carbon and other ice core aerosol records in the Arctic for GCM evaluation,  
809 *Atmos. Environ.*, 44, 2665–2666, <https://doi.org/10.1016/j.atmosenv.2010.04.004>, 2010.

810 McConnell, J. R., Edwards, R., Kok, G. L., Flanner, M. G., Zender, C. S., Saltzman, E. S., Banta, J. R., Pasteris, D. R., Carter,  
811 M. M., and Kahl, J. D.: 20th-century industrial black carbon emissions altered Arctic climate forcing, *Science*, 317, 1381–  
812 1384, 10.1126/science.1144856, 2007.

813 Mori, T., Moteki, N., Ohata, S., Koike, M., Goto-Azuma, K., Miyazaki, Y., and Kondo, Y.: Improved technique for measuring  
814 the size distribution of black carbon particles in liquid water, *Aerosol Sci. Tech.*, 50, 242–254,  
815 10.1080/02786826.2016.1147644, 2016.

816 Mori, T., Goto-Azuma, K., Kondo, Y., Ogawa-Tsukagawa, Y., Miura, K., Hirabayashi, M., Oshima, N., Koike, M., Kupiainen,  
817 K., Moteki, N., Ohata, S., Sinha, P. R., Sugiura, K., Aoki, T., Schneebeli, M., Steffen, K., Sato, A., Tsushima, A., Makarov,



818 V., Omiya, S., Sugimoto, A., Takano, S., and Nagatsuka, N.: Black Carbon and Inorganic Aerosols in Arctic Snowpack, J.  
819 Geophys. Res.-Atmos., 124, 13325–13356, 10.1029/2019jd030623, 2019.

820 Moseid, K. O., Schulz, M., Eichler, A., Schwikowski, M., McConnell, J. R., Olivié, D., Criscitiello, A. S., Kreutz, K. J., and  
821 Legrand, M.: Using ice cores to evaluate CMIP6 aerosol concentrations over the historical era, J. Geophys. Res.-Atmos.,  
822 127, e2021JD036105, <https://doi.org/10.1029/2021JD036105>, 2022.

823 Mosher, B. W., Winkler, P., and Jaffrezo, J.-L.: Seasonal aerosol chemistry at Dye 3, Greenland, Atmos. Environ. A-Gen., 27,  
824 2761–2772, [https://doi.org/10.1016/0960-1686\(93\)90308-L](https://doi.org/10.1016/0960-1686(93)90308-L), 1993.

825 Moteki, N.: Climate-relevant properties of black carbon aerosols revealed by in situ measurements: a review, Prog. Earth  
826 Planet. Sci., 10, 12, 10.1186/s40645-023-00544-4, 2023.

827 ~~[Moteki, N. and Kondo, Y.: Dependence of laser-induced incandescence on physical properties of black carbon aerosols:  
828 Measurements and theoretical interpretation, Aerosol Sci. Tech., 44, 663–675, 10.1080/02786826.2010.484450, 2010.  
829 Muggeo, V. M. R.: Estimating regression models with unknown break-points, Stat. Med., 22, 3055–  
830 3071, <https://doi.org/10.1002/sim.1545>, 2003.](#)~~

831

832 Nagatsuka, N., Goto-Azuma, K., Tsushima, A., Fujita, K., Matoba, S., Onuma, Y., Dallmayr, R., Kadota, M., Hirabayashi, M.,  
833 Ogata, J., Ogawa-Tsukagawa, Y., Kitamura, K., Minowa, M., Komuro, Y., Motoyama, H., and Aoki, T.: Variations in  
834 mineralogy of dust in an ice core obtained from northwestern Greenland over the past 100 years, Clim. Past, 17, 1341–1362,  
835 10.5194/cp-17-1341-2021, 2021.

836 ~~[Nagatsuka, N., Goto-Azuma, K., Fujita, K., Komuro, Y., Hirabayashi, M., Ogata, J., Fukuda, K., Ogawa-Tsukagawa, Y.,  
837 Kitamura, K., Yonekura, A., Nakazawa, F., Onuma, Y., Kurita, N., Rasmussen, S. O., Sinnl, G., Popp, T. J., and Dahl-  
838 Jensen, D.: Regional variations in mineralogy of dust in ice cores obtained from northeastern and northwestern Greenland  
839 over the past 100 years, EGU sphere, 2023, 1–32, 10.5194/egusphere-2023-1666, 2023.](#)~~

840 ~~[Neem-NEEM](#) Community Members: Eemian interglacial reconstructed from a Greenland folded ice core, Nature, 493, 489–  
841 494, 10.1038/nature11789, 2013.~~

842 Ohata, S., Moteki, N., Schwarz, J., Fahey, D., and Kondo, Y.: Evaluation of a method to measure black carbon particles  
843 suspended in rainwater and snow samples, Aerosol Sci. Technol., 47, 1073–1082, 10.1080/02786826.2013.824067, 2013.

844 Osmont, D., Wendl, I. A., Schmidely, L., Sigl, M., Vega, C. P., Isaksson, E., and Schwikowski, M.: An 800-year high-  
845 resolution black carbon ice core record from Lomonosovfonna, Svalbard, *Atmos. Chem. Phys.*, 18, 12777–12795,  
846 10.5194/acp-18-12777-2018, 2018.

847 Parvin, F., Seki, O., Fujita, K., Iizuka, Y., Matoba, S., Ando, T., and Sawada, K.: Assessment for paleoclimatic utility of  
848 biomass burning tracers in SE-Dome ice core, Greenland, *Atmos. Environ.*, 196, 86–94,  
849 <https://doi.org/10.1016/j.atmosenv.2018.10.012>, 2019.

850 [Petzold, A., Ogren, J. A., Fiebig, M., Laj, P., Li, S.-M., Baltensperger, U., Holzner-Popp, T., Kinne, S., Pappalardo, G.,](#)  
851 [Sugimoto, N., Wehrli, C., Wiedensohler, A., and Zhang, X.-Y.: Recommendations for reporting “black carbon”](#)  
852 [measurements. \*Atmos. Chem. Phys.\*, 13, 8365–8379, 10.5194/acp-13-8365-2013, 2013.](#)

853 Pokhrel, A., Kawamura, K., Kunwar, B., Ono, K., Tsushima, A., Seki, O., Matoba, S., and Shiraiwa, T.: Ice core records of  
854 levoglucosan and dehydroabietic and vanillic acids from Aurora Peak in Alaska since the 1660s: A proxy signal of biomass-  
855 burning activities in the North Pacific Rim, *Atmos. Chem. Phys.*, 20, 597–612, 10.5194/acp-20-597-2020, 2020.

856 Power, M. J., Marlon, J. R., Bartlein, P. J., and Harrison, S. P.: Fire history and the Global Charcoal Database: A new tool for  
857 hypothesis testing and data exploration, *Palaeogeogr. Palaeoclimatol.*, 291, 52–59, <http://dx.doi.org/10.1016/j.palaeo.2009.09.014>,  
858 2010.

859 Power, M., Mayle, F., Bartlein, P., Marlon, J., Anderson, R., Behling, H., Brown, K., Carcaillet, C., Colombaroli, D., Gavin,  
860 D., Hallett, D., Horn, S., Kennedy, L., Lane, C., Long, C., Moreno, P., Paitre, C., Robinson, G., Taylor, Z., and Walsh, M.:  
861 Climatic control of the biomass-burning decline in the Americas after ad 1500, *The Holocene*, 23, 3–13,  
862 10.1177/0959683612450196, 2013.

863 Qi, L. and Wang, S.: Sources of black carbon in the atmosphere and in snow in the Arctic, *Sci. Total Environ.*, 691, 442–454,  
864 <https://doi.org/10.1016/j.scitotenv.2019.07.073>, 2019.

865 Rantanen, M., Karpechko, A. Y., Lipponen, A., Nordling, K., Hyvärinen, O., Ruosteenoja, K., Vihma, T., and Laaksonen, A.:  
866 The Arctic has warmed nearly four times faster than the globe since 1979, *Comm. Earth Environ.*, 3, 168, 10.1038/s43247-  
867 022-00498-3, 2022.

868 Rasmussen, S. O., Seierstad, I. K., Andersen, K. K., Bigler, M., Dahl-Jensen, D., and Johnsen, S. J.: Synchronization of the  
869 NGRIP, GRIP, and GISP2 ice cores across MIS 2 and palaeoclimatic implications, *Quaternary Sci. Rev.*, 27, 18–28,  
870 <http://dx.doi.org/10.1016/j.quascirev.2007.01.016>, 2008.

871 Rubino, M., D'Onofrio, A., Seki, O., and Bendle, J. A.: Ice-core recodes of biomass burning, *The Anthropocene Rev.*, 3, 140-  
872 162, <https://journals.sagepub.com/doi/abs/10.1177/2053019615605117>, 2016.

873 Ruppel, M. M., Isaksson, I., Ström, J., Beaudon, E., Svensson, J., Pedersen, C. A., and Korhola, A.: Increase in elemental  
874 carbon values between 1970 and 2004 observed in a 300-year ice core from Holtedahlfonna (Svalbard), *Atmos. Chem. Phys.*,  
875 14, 11447–11460, [10.5194/acp-14-11447-2014](https://doi.org/10.5194/acp-14-11447-2014), 2014.

876 Savarino, J. and Legrand, M.: High northern latitude forest fires and vegetation emissions over the last millennium inferred  
877 from the chemistry of a central Greenland ice core, *J. Geophys. Res.-Atmos.*, 103, 8267–8279, [10.1029/97jd03748](https://doi.org/10.1029/97jd03748), 1998.

878 Schmeisser, L., Backman, J., Ogren, J. A., Andrews, E., Asmi, E., Starkweather, S., Uttal, T., Fiebig, M., Sharma, S.,  
879 Eleftheriadis, K., Vratolis, S., Bergin, M., Tunved, P., and Jefferson, A.: Seasonality of aerosol optical properties in the  
880 Arctic, *Atmos. Chem. Phys.*, 18, 11599–11622, [10.5194/acp-18-11599-2018](https://doi.org/10.5194/acp-18-11599-2018), 2018.

881 Schwarz, J. P., Gao, R. S., Perring, A. E., Spackman, J. R., and Fahey, D. W.: Black carbon aerosol size in snow, *Sci. Rep.*, 3,  
882 1356, [10.1038/srep01356](https://doi.org/10.1038/srep01356), 2013.

883 Sharma, S., Andrews, E., Barrie, L. A., Ogren, J. A., and Lavoué, D.: Variations and sources of the equivalent black carbon in  
884 the high Arctic revealed by long-term observations at Alert and Barrow: 1989–2003, *J. Geophys. Res.-Atmos.*, 111,  
885 <https://doi.org/10.1029/2005JD006581>, 2006.

886 Sharma, S., Barrie, L. A., Magnusson, E., Brattström, G., Leaitch, W. R., Steffen, A., and Landsberger, S.: A factor and trends  
887 analysis of multidecadal lower tropospheric observations of Arctic aerosol composition, black carbon, ozone, and mercury  
888 at Alert, Canada, *J. Geophys. Res.-Atmos.*, 124, 14133–14161, <https://doi.org/10.1029/2019JD030844>, 2019.

889 Sharma, S., Ishizawa, M., Chan, D., Lavoué, D., Andrews, E., Eleftheriadis, K., and Maksyutov, S.: 16-year simulation of  
890 Arctic black carbon: Transport, source contribution, and sensitivity analysis on deposition, *J. Geophys. Res.-Atmos.*, 118,  
891 943–964, <https://doi.org/10.1029/2012JD017774>, 2013.

892 Shindell, D. and Faluvegi, G.: Climate response to regional radiative forcing during the twentieth century, *Nat. Geosci.*, 2,  
893 294–300, [10.1038/ngeo473](https://doi.org/10.1038/ngeo473), 2009.

894 ~~Sigl, M., McConnell, J. R., Layman, L., Maselli, O., McGwire, K., Pasteris, D., Dahl Jensen, D., Steffensen, J. P., Vinther, B.,~~  
895 ~~Edwards, R., Mulvaney, R., and Kipfstuhl, S.: A new bipolar ice core record of volcanism from WAIS Divide and NEEM~~  
896 ~~and implications for climate forcing of the last 2000 years, *J. Geophys. Res. Atmos.*, 118, 1151–1169,~~  
897 ~~[10.1029/2012jd018603](https://doi.org/10.1029/2012jd018603), 2013.~~

898 Sinnl, G., Winstrup, M., Erhardt, T., Cook, E., Jensen, C. M., Svensson, A., Vinther, B. M., Muscheler, R., and Rasmussen, S.  
899 O.: A multi-ice-core, annual-layer-counted Greenland ice-core chronology for the last 3800 years: GICC21, *Clim. Past*, 18,  
900 1125–1150, 10.5194/cp-18-1125-2022, 2022.

901 Skakun, R. Whitman, E., Little, J. M., and Parisien, M.-A.: Area burned adjustments to historical wildfires in Canada, *Environ.*  
902 *Res. Lett.* 16 064014, 2021.

903 Stein, A. F., Draxler, R. R., Rolph, G. D., Stunder, B. J. B., Cohen, M. D., and Ngan, F.: NOAA’s HYSPLIT atmospheric  
904 transport and dispersion modeling system, *B. Am. Meteorol. Soc.*, 96, 2059–2077, [https://doi.org/10.1175/BAMS-D-14-](https://doi.org/10.1175/BAMS-D-14-00110.1)  
905 00110.1, 2015.

906 Stephens, M., Turner, N., and Sandberg, J.: Particle identification by laser-induced incandescence in a solid-state laser cavity,  
907 *Appl. Opt.*, 42, 3726–3736, 10.1364/AO.42.003726, 2003.

908 van Marle, M. J. E., Kloster, S., Magi, B. I., Marlon, J. R., Daniiau, A. L., Field, R. D., Arneth, A., Forrest, M., Hantson, S.,  
909 Kehrwald, N. M., Knorr, W., Lasslop, G., Li, F., Mangeon, S., Yue, C., Kaiser, J. W., and van der Werf, G. R.: Historic  
910 global biomass burning emissions for CMIP6 (BB4CMIP) based on merging satellite observations with proxies and fire  
911 models (1750–2015), *Geosci. Model Dev.*, 10, 3329–3357, 10.5194/gmd-10-3329-2017, 2017.

912 Vinther, B. M., Buchardt, S. L., Clausen, H. B., Dahl-Jensen, D., Johnsen, S. J., Fisher, D. A., Koerner, R. M., Raynaud, D.,  
913 Lipenkov, V., Andersen, K. K., Blunier, T., Rasmussen, S. O., Steffensen, J. P., and Svensson, A. M.: Holocene thinning of  
914 the Greenland ice sheet, *Nature*, 461, 385–388, 10.1038/nature08355, 2009.

915 Wang, M., Xu, B., Kaspari, S. D., Gleixner, G., Schwab, V. F., Zhao, H., Wang, H., and Yao, P.: Century-long record of black  
916 carbon in an ice core from the Eastern Pamirs: Estimated contributions from biomass burning, *Atmos. Environ.*, 115, 79–  
917 88, <https://doi.org/10.1016/j.atmosenv.2015.05.034>, 2015.

918 Wang, D., Guan, D., Zhu, S., Kinnon, M. M., Geng, G., Zhang, Q., Zheng, H., Lei, T., Shao, S., Gong, P., and Davis, S. J.:  
919 Economic footprint of California wildfires in 2018, *Nat. Sustain.*, 4, 252–260, 10.1038/s41893-020-00646-7, 2021.

920 Warren, S. G.: Light-Absorbing Impurities in Snow: A Personal and Historical Account, *Front. Earth Sci.* 6:250. doi:  
921 10.3389/feart.2018.00250, 2019.

922 Wendl, I. A., Menking, J. A., Färber, R., Gysel, M., Kaspari, S. D., Laborde, M. J. G., and Schwikowski, M.: Optimized  
923 method for black carbon analysis in ice and snow using the Single Particle Soot Photometer, *Atmos. Meas. Tech.*, 7, 2667–  
924 2681, 10.5194/amt-7-2667-2014, 2014.

925 Whitlow, S., Mayewski, P., Dibb, J., Holdsworth, G., and Twickler, M.: An ice-core-based record of biomass burning in the  
926 Arctic and Subarctic, 1750–1980, *Tellus B*, 46, 234–242, <https://doi.org/10.1034/j.1600-0889.1994.t01-2-00006.x>, 1994.

927 Whitman, E., Parisien, M.-A., Thompson, D. K., Hall, R. J., Skakun, R. S., and Flannigan, M. D.: Variability and drivers of  
928 burn severity in the northwestern Canadian boreal forest, *Ecosphere*, 9, e02128, <https://doi.org/10.1002/ecs2.2128>, 2018.

929 Wiscombe, W. J. and Warren, S. G.: A model for the spectral albedo of snow. I: Pure snow, *J. Atmos. Sci.*, 37, 2712–2733,  
930 [doi:10.1175/1520-0469\(1980\)037<2712:AMFTSA>2.0.CO;2](https://doi.org/10.1175/1520-0469(1980)037<2712:AMFTSA>2.0.CO;2), 1980.

931 Zdanowicz, C. M., Proemse, B. C., Edwards, R., Feiteng, W., Hogan, C. M., Kinnard, C., and Fisher, D.: Historical black  
932 carbon deposition in the Canadian High Arctic: a 250-year long ice-core record from Devon Island, *Atmos. Chem. Phys.*,  
933 18, 12345–12361, [10.5194/acp-18-12345-2018](https://doi.org/10.5194/acp-18-12345-2018), 2018.

934 Zennaro, P., Kehrwald, N., McConnell, J. R., Schüpbach, S., Maselli, O. J., Marlon, J., Vallelonga, P., Leuenberger, D.,  
935 Zangrando, R., Spolaor, A., Borrotti, M., Barbaro, E., Gambaro, A., and Barbante, C.: Fire in ice: two millennia of boreal  
936 forest fire history from the Greenland NEEM ice core, *Clim. Past*, 10, 1905–1924, [10.5194/cp-10-1905-2014](https://doi.org/10.5194/cp-10-1905-2014), 2014.

937

**Figure A1: Map showing 21 regions used for calculating the regional contributions in backward trajectory analysis.**

**ME: Middle East, AT: Antarctica, AUS: Australia and New Zealand, SAM: South America, AF: Africa, EA: China and East Asia, EU: Europe, GrIS: Greenland Ice Sheet, SEA: Southeast Asia, SA: South Asia, CA: Central Asia, RUS: Russia, NA: North America, ATO: Antarctic Ocean, SPO: South Pacific Ocean, INO: Indian Ocean, NPO: North Pacific Ocean, SAO: South Atlantic Ocean, NAO: North Atlantic Ocean, AO: Arctic Ocean, IC: Iceland.**

